DEVELOPMENT OF AFFINITY GRID MATERIALS FOR CRYOELCTRONIC MICROSCOPY

by

Md Rejaul Hoq

A Thesis

Submitted to the Faculty of Purdue University

In Partial Fulfillment of the Requirements for the degree of

Master of Science

Department of Chemistry

West Lafayette, Indiana

May 2019

THE PURDUE UNIVERSITY GRADUATE SCHOOL
STATEMENT OF COMMITTEE APPROVAL

Dr. David H. Thompson, Chair
Department of Chemistry
Dr. Mingji Dai
Department of Chemistry
Dr. Angeline Lyon
Department of Chemistry

Approved by:
Dr. Christine Hrycyna
Head of the Graduate Program

This thesis is dedicated to my late father who didn't stay long enough in this beautiful world.

TABLE OF CONTENTS

LIST OF FIGURES

ABSTRACT

Author: Hoq, Md Rejaul. MS
Institution: Purdue University
Degree Received: May 2019
Title: Development of Affinity Grid Materials for Cryoelctronic-Microscopy
Committee Chair: David H. Thompson

Cryogenic transmission electron microscopy (cryoEM) has become an increasingly common tool for determining structures of proteins and protein complex at near atomic resolution. We seek to determine the structure of p97 by cryoEM using an affinity capture approach that employs a family of novel synthetic lipids bearing water soluble PEG units and known high affinity inhibitor molecules at the distal end of the polymer. A library of inhibitor modified affinity lipopolymers of 5000 KD PEG molecular weights were synthesized. The inhibitor modified lipid coated grids were used to capture p97. The reconstruction of p97 revealed the structure at dimeric state at 3.64 Å and monomeric state at 4.33 Å. A PEG unit composed of 20000 KD molecular weight based polyrotaxane containing NTA ligand as affinity tag has been synthesized, used to concentrate 6x-his tagged p97 on TEM which also enabled to see all 3D orientation of the target particles and an initial model of 10.64 Å resolution of p97 structure was resolved.

CHAPTER 1. INTRODUCTION

1.1 Challenges in protein's structure determination

Researcher has been using X-ray crystallography, nuclear magnetic resonance, and electron microscope to elucidate high resolution three-dimensional structure of numerous biomolecular complexes. Generally, computer assisted software generate active site of protein, on basis of which targeted drug molecules are designed to synthesize. Any of above method doesn't permit to observe atom to atom single bond to elucidate electron density map of biomolecule and different orientation of atoms in biomolecules.

X-ray crystallography has been considered as most widely used technique to determine three-dimensional structure of different biomolecules. According to this procedure, the proteins are settling down in very repetitive pattern where three-dimensional crystal are grown. The high quality three-dimensional crystals produce electron density map through x-ray diffraction pattern of each crystal to elucidate three-dimensional structure of biomolecules[1]. The supersaturated solution of biomolecule is condition for growing crystal. The different types of inorganic saults such as NaCl, $CaCl_2$, KCl, or polymeric precipitants such as polyethylene glycol and volatile organic solvent such as ethanol, methanol chloroform etc. are used to induce supersaturation and concentrate the solution. The crystal growth of biomolecule is limited to have very intermolecular interaction for extended lattice formation. Protein exhibits complex phase diagram are very sensitive to different condition of solution such as concentration, pH, salinity etc. which make difficult protein highly pure for proteolytic degradation. The protein crystallization is highly dependent on different experimental variables such as concentration, pH, salinity etc. Generally, most well-ordered protein's crystal has been shown well separated nucleation and crystal growth phases. Protein tends to show impaired crystallization for lower rate of intermolecular contacts

which make every protein unique. The misfolded states of proteins can be formed by frequent conformational flexibility. It has been seen that it is hard to concentrate protein's solution and higher content of water makes crystal so fragile. So, the larger and complex macromolecule is less likely to form well-ordered crystal. Some biomolecules could be highly unstable to different condition for crystallization or precipitated for denaturation. The dynamic nature of lipid membrane tends to prevent crystallization[2-4].

Nuclear Magnetic Resonance (NMR) spectroscopy has also long been used to determine non-crystallizable bio-macromolecule structure up to high resolution which enables to disclose relative disorder by analyzing NMR peak in desired regions. One big disadvantage is that NMR requires more than one milligram of sample and highly concentrated sample[5, 6].

In the meanwhile, Single-particle cryogenic electron microscopy (cryo-EM) is a rapidly emerging biological structure determination tools which is now able to produce around 2 Å resolution structure macromolecules[7-11]. It has been seen that thousands of images of single particles are collected to achieve higher resolution structure[12]. Those structure are determined by collected and average images from many types of biomaterials coated and noncoated TEM grids preparation that specifically/randomly bind protein in different orientation.

Sample needs to be frozen in a thin film of vitreous ice in single particles cryo-EM, followed by imaging by the transmission electron microscope (TEM) for two-dimensional projection images of the target particles. First, individual particle's orientation is measured computationally, a 3-D model is subsequently generated on basis of target particle's structural interpretation.

Single particle cryo-EM has many advantages over X-ray crystallography. First, it is valid to a range of target proteins which are refractory to crystallization and can solve high-resolution structures more quickly using lower copy of target biomolecules. Secondly, with cryo-EM, target

macromolecules are preserved at close-to-native conditions and thus the elucidated structures could represent more closely to the biological states.

Moreover, in cryo-EM, a single set of targeted particles can resolve multiple active conformation[13]. These superior characteristics of cryo-EM made it more advanced, efficient, promising, and informative structural biology tool, which could benefit structural studies of different known and unknown macromolecules and structure-based drug design.

Although single particle cryo-EM doesn't require high amount with high concentration, still there are lot of challenges in dealing rare sample to reach standard cryo-EM approach, such as lower copy, low yield, low concentration and labile structure of target biomolecules which cannot survive standard biochemical purification[10, 14].

1.2 Our Methods in Addressing Drawbacks to High Resolution Cryo-EM Imaging

1.2.1 Inhibitor Modified Lipid Monolayer Affinity Grid Approach

In an attempt to optimize cryo-EM grid preparation and also tackle challenging samples to cryo-EM, we have explored the affinity based cryo-EM approach. More Specifically, we have designed inhibitor-based affinity cryo-EM technique that provides an easy to use, effort-saving specimen preparation approach for the single particles cryo-EM structural studies of p97.

Therefore, we seek to determine the structure of p97 by cryo-EM using an affinity capture approach that employs a family of novel synthetic lipids bearing water soluble PEG units and known high affinity inhibitor molecules at the distal end of the polymer. The project objectives are verification of the inhibitor capture concept using a well characterized p97 inhibitor. We addressed these challenges by focusing on determining the near-atomic resolution structure of inhibitor-free his6-p97. This is served as a template to identify regions of the protein with additional density due to inhibitor binding. We propose to elucidate the structure of p97 in complex with four different

inhibitors at 3.64 Å resolutions by cryoEM to identify the p97 amino acids that are interacting with the inhibitors in the binding pocket. We utilize established methods of the structural elucidation of p97[15] and adapt them to the preparation of inhibitor-modified grids for high resolution single particle reconstruction analysis.

1.2.2 Polyrotaxane Based Rod Shaped Scaffold approach

We have developed polytrioxane based novel materials to accelerate cryo-EM single particle reconstruction (SPR) productivity that will concentrate the biological sample onto a rod-like scaffold prior to deposition onto the TEM grid. Our strategy integrates macromolecule containing affinity ligand synthesis and characterization to develop rod-like materials that actively discourage non-specific protein adsorption, while enhancing the capture and random presentation of target proteins on the rod-like scaffold. In this project, α-cyclodextrins (α- CD) are threaded onto a linear polymer polyethylene glycol (PEG) chains bound to nitrilotriacetic acid (NTA) ligands, CD was conjugated NTA ligand which was used to capture his-tagged protein. We addressed that the antifouling properties of long PEG chain inhibit nonspecific protein adsorption, with specific capture provided by affinity NTA:Ni^{2+}:polyhistidine recognition on the polymer, to concentrate His-tagged p97 on a spatially well-defined scaffold for cryoEM SPR. The anticipated advantages of CD Polyrotaxanes (PR) are lateral and rotational mobility of the threaded macrocycles that enable their adaptation to the steric demands of the adsorbate. Our result from negative stained and cryo-EM imaging indicates more unbiased orientations of the concentrated His-tagged p97, which is important for high-resolution structure elucidation with cryoEM SPR. We have generated an initial model of p97 captured at 10.56 Å, more effort are given to get higher resolution p97 structure.

1.3 References

1. Krissinel, E.; Henrick, K., Inference of macromolecular assemblies from crystalline state. *J Mol Biol* **2007,** *372* (3), 774-97.

2. Rossmann, M. G.; Morais, M. C.; Leiman, P. G.; Zhang, W., Combining X-ray crystallography and electron microscopy. *Structure* **2005,** *13* (3), 355-62.

3. Fujiyoshi, Y., Electron crystallography for structural and functional studies of membrane proteins. *Journal of electron microscopy* **2011,** *60 Suppl 1*, S149-59.

4. Wisedchaisri, G.; Reichow, S. L.; Gonen, T., Advances in structural and functional analysis of membrane proteins by electron crystallography. *Structure* **2011,** *19* (10), 1381-93.

5. Renault, M.; Cukkemane, A.; Baldus, M., Solid-state NMR spectroscopy on complex biomolecules. *Angew Chem Int Ed Engl* **2010,** *49* (45), 8346-57.

6. Wider, G.; Wuthrich, K., NMR spectroscopy of large molecules and multimolecular assemblies in solution. *Curr Opin Struct Biol* **1999,** *9* (5), 594-601.

7. Belnap, D. M., Electron Microscopy and Image Processing: Essential Tools for Structural Analysis of Macromolecules. *Current Protocols in Protein Science* **2015,** *82* (1), 17.2.1-17.2.61.

8. Frank, J., Generalized single-particle cryo-EM--a historical perspective. *Microscopy (Oxf)* **2016,** *65* (1), 3-8.

9. Kelly, D. F.; Dukovski, D.; Walz, T., Strategy for the use of affinity grids to prepare non-His-tagged macromolecular complexes for single-particle electron microscopy. *Journal of molecular biology* **2010,** *400* (4), 675-681.

10. Skiniotis, G.; Southworth, D. R., Single-particle cryo-electron microscopy of macromolecular complexes. *Microscopy (Oxf)* **2016,** *65* (1), 9-22.

11. Bartesaghi, A.; Merk, A.; Banerjee, S.; Matthies, D.; Wu, X.; Milne, J. L.; Subramaniam, S., 2.2 A resolution cryo-EM structure of beta-galactosidase in complex with a cell-permeant inhibitor. *Science* **2015,** *348* (6239), 1147-51.

12. Bartesaghi, A., 2.2 A resolution cryo-EM structure of [beta]-galactosidase in complex with a cell-permeant inhibitor. *Science* **2015,** *348*, 1147-1151.

13. Bai, X.-c.; Rajendra, E.; Yang, G.; Shi, Y.; Scheres, S. H. W., Sampling the conformational space of the catalytic subunit of human γ-secretase. *eLife* **2015,** *4*, e11182.

14. Orlova, E. V.; Saibil, H. R., Structural analysis of macromolecular assemblies by electron microscopy. *Chem Rev* **2011,** *111* (12), 7710-48.

15. Banerjee, S.; Bartesaghi, A.; Merk, A.; Rao, P.; Bulfer, S. L.; Yan, Y.; Green, N.; Mroczkowski, B.; Neitz, R. J.; Wipf, P.; Falconieri, V.; Deshaies, R. J.; Milne, J. L.; Huryn, D.; Arkin, M.; Subramaniam, S., 2.3 Å resolution cryo-EM structure of human p97 and mechanism of allosteric inhibition. *Science* **2016,** *351*, 871-875.

CHAPTER 2. DEVELOPMENT OF INHIBITOR-MODIFIED AFFINITY GRID FOR CRYOELECTRON MICROSCOPY

2.1 Project Overview

Cryogenic transmission electron microscopy (cryo-EM) has become an increasingly common tool for determining structures of proteins and protein complex at near atomic resolution approaching around 2 Å. Although cryo-EM involves lower quantity of sample than other traditional techniques such as NMR, X-ray crystallography, sample preparation remains challenging for specimens that are low yielding, in low copy number or short lived. Recent progress in affinity grid approach in cryo-EM has started solving these challenges by concentrating and purification of rare samples onto the TEM grid in one step. Typically, this approach requires genetic engineering of the protein sample such as tagging with histidine which is another big challenge[1-4]. Therefore, this project seeks to develop new inhibitor-modified affinity cryo-EM grid that can directly concentrate non-engineered samples from cell lysates on to the grid surface.

The p97 protein complex is an AAA-ATPase with multiple cellular functions, including membrane fusion, golgi reassembly, cell cycle regulation and ubiquitin dependent protein degradation of misfolded proteins. It is a heterodimer of hexameric assemblies comprised of D1 and D2 domains, with its ATPase activity requiring the assembly of the D2 domain. p97 is a well-known ATPase protein that binds with multiple adapter proteins including deubiquitinating enzymes, ubiquitin-binding adaptors and ligases[5-10]. The p97 hexamer also has an ATP-hydrolysis-dependent moveable arginine and, the subunits are arranged in ring way with small hydrophobic pore in the middle. Mutations in p97 are linked to disorders caused by the disruption of the endoplasmic reticulum associated protein degradation (ERAD) pathway. In the ERAD process, p97 extracts

misassembled or misfolded proteins from the ER and transfer them into the cytosol, where ERAD substrate protein degradation is mediated by the ubiquitin proteasome system (UPS). .

The central role that p97 plays in protein quality control makes it an attractive target for anticancer drug development. Overexpression of p97 is also associated with different cancer cells[5]. A functional deficiency of p97 contributes to the unfolded protein response and cell death, making it's inhibition an attractive target for cancer drug development.

A few classes of inhibitors have been developed that operate via an allosteric or competitive mechanism to impair p97 ATPase activity[11-20]. Recently, a series of phenyl indole derivatives have been developed having binding constants in the low nM range as allosteric inhibitors, one of these compounds has been used to determine the cryo-EM structure of the p97-inhibitor complex at 2.3 Å resolution [20]. It has been discovered that the indole based inhibitor binds between the D1 and D2 domains of p97[21]. As p97 is homo-hexameric protein complex with six binding sites, there are many important features of this protein that remain unknown, particularly with respect to how domains react with sub stoichiometric inhibitor concentration.

The goal of this project is to develop a method to determine the structure of p97 by cryo-EM using an inhibitor as a ligand bound via a novel synthetic lipid bearing water soluble PEG units and hydrophobic tails. We seek to identify regions of the protein with additional density due to inhibitor binding at 3.64 Å resolution by cryoEM to identify the p97 amino acids that are interacting with the inhibitors in the binding pocket. The overall scheme of the project is shown in Figure 1.

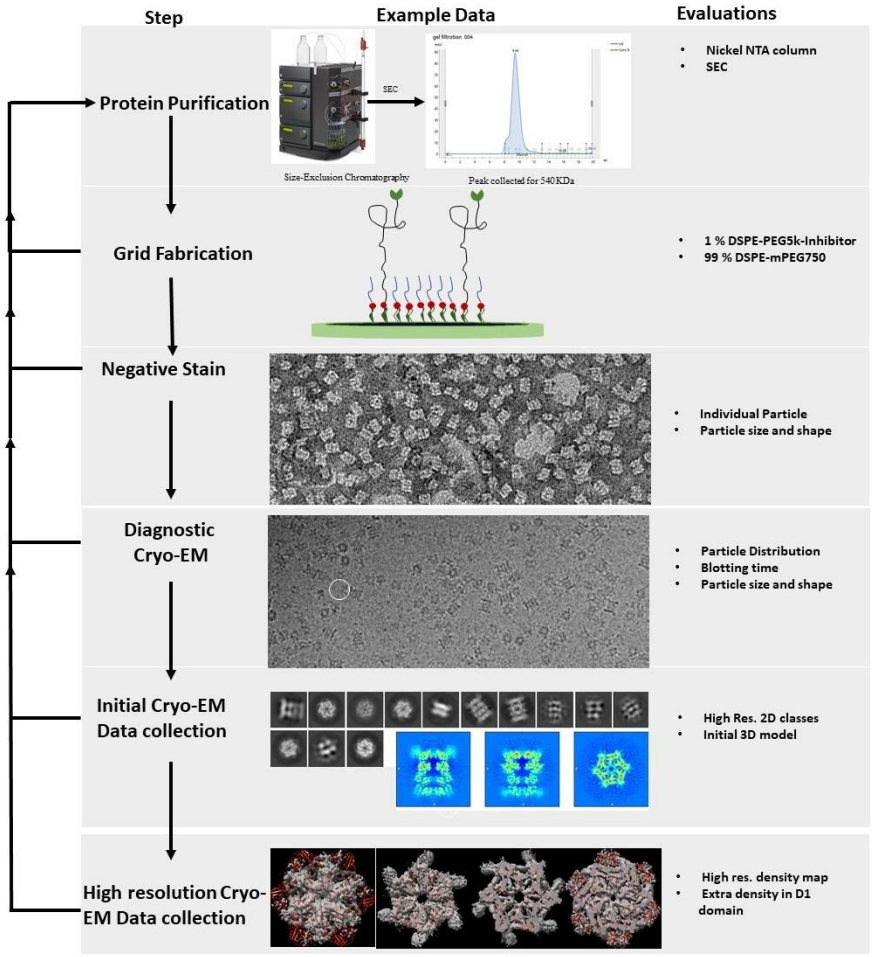

Figure 1: A systematic approach to 3D reconstruction is shown. In the left column, all steps are listed. In middle column, example data are shown for the inhibitor affinity grid approach for p97(Scale bar are not shown). The right column shows the specific experiment performed.

2.2 Design of Inhibitor Modified Affinity Grid Approach

A novel method has been developed to introduce a new concept for affinity capture on a TEM grid surface by using a Lipid-PEG conjugate inhibitor as bait. The main advantages of this approach are that genetic engineering of the protein target is not required (e.g. his tag and large antibodies are not required for specific capture). Four inhibitor conjugates composed of a flexible water-soluble polyethylene glycol 5000 (PEG 5k) unit attached to 1,2-distearoyl-*sn*-glycero-3-phosphoethanolamine (DSPE) at one end of the polymer were synthesized; these four different

conjugates provided a high affinity interaction with p97 and concentrate it at the grid surface (Figure-1). A long PEG spacer is used in this case to avoid potential preferred orientations of p97 that may occur if the tether length between the protein and surface is too short.

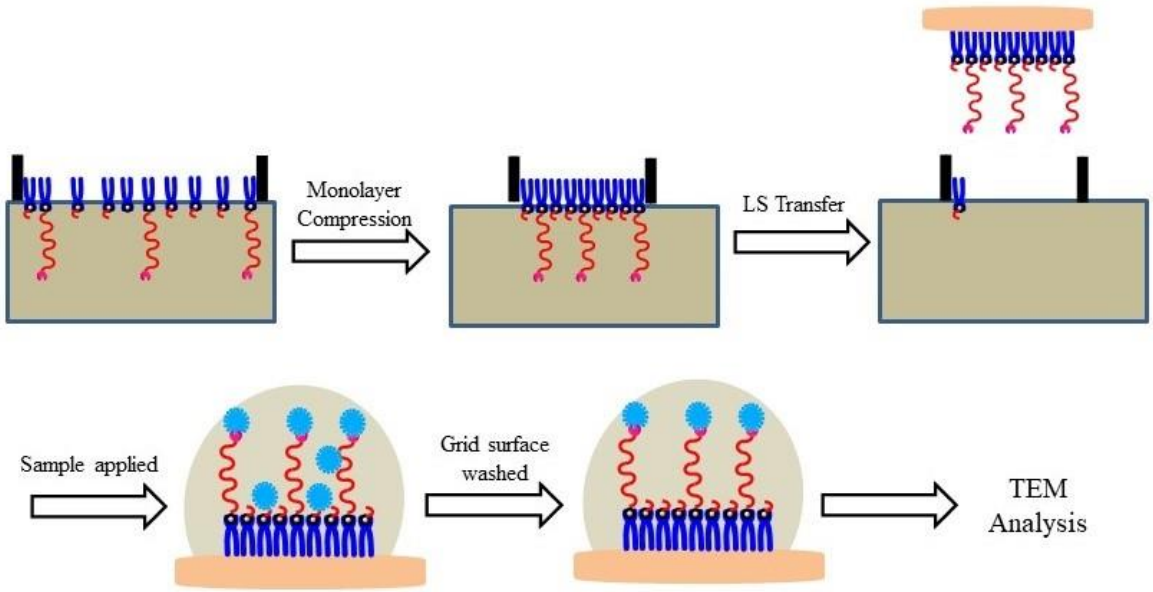

Figure 2: Conceptual diagram showing inhibitor modified TEM grid fabrication and capture of p97

In the first step, DSPE-PEG(5k)-DBCO was synthesized from DSPE-PEG(5k)-NH_2 and NHS-DBCO. The drug conjugate was then obtained by strain-induced 'click' reaction between the

DSPE-PEG(5k)-DBCO derivative and the azide-modified drug candidates. The library of four lipopolymers inhibitors are shown in Figure 2.

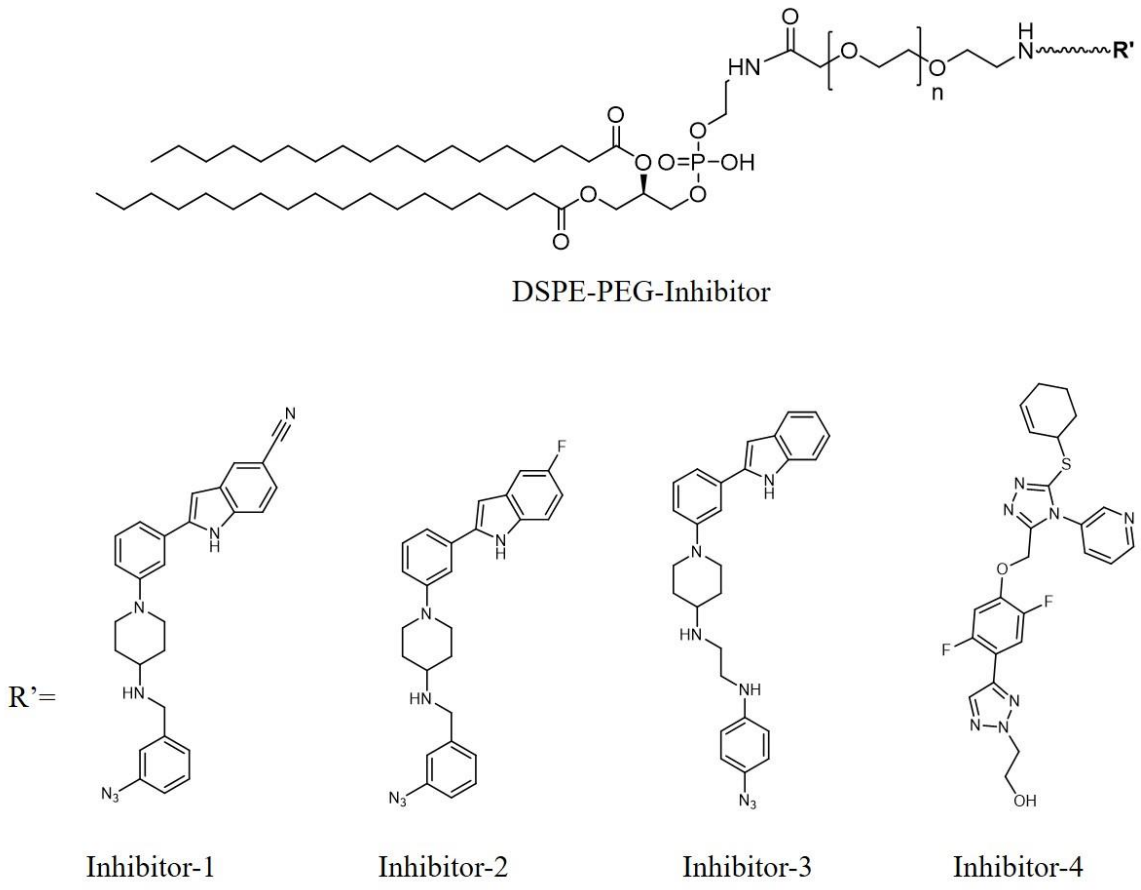

Figure 3: Chemical structures of inhibitor-modified lipopolymer library

2.3 Experimental

2.3.1 Synthesis and Characterization of Affinity Lipopolymer Constructs

1,2-Distearoyl-*sn*-glycero-3-phosphoethanolamine modified with PEG-NH_2 (molecular weight 5000 Dalton) was treated with DBCO-NHS in $CHCl_3$ in the presence of DIPEA. The resulting DSPE-PEG-DBCO intermediate was treated with azide containing inhibitor to make inhibitor modified DSPE-PEG-Inhibitor as described bellow

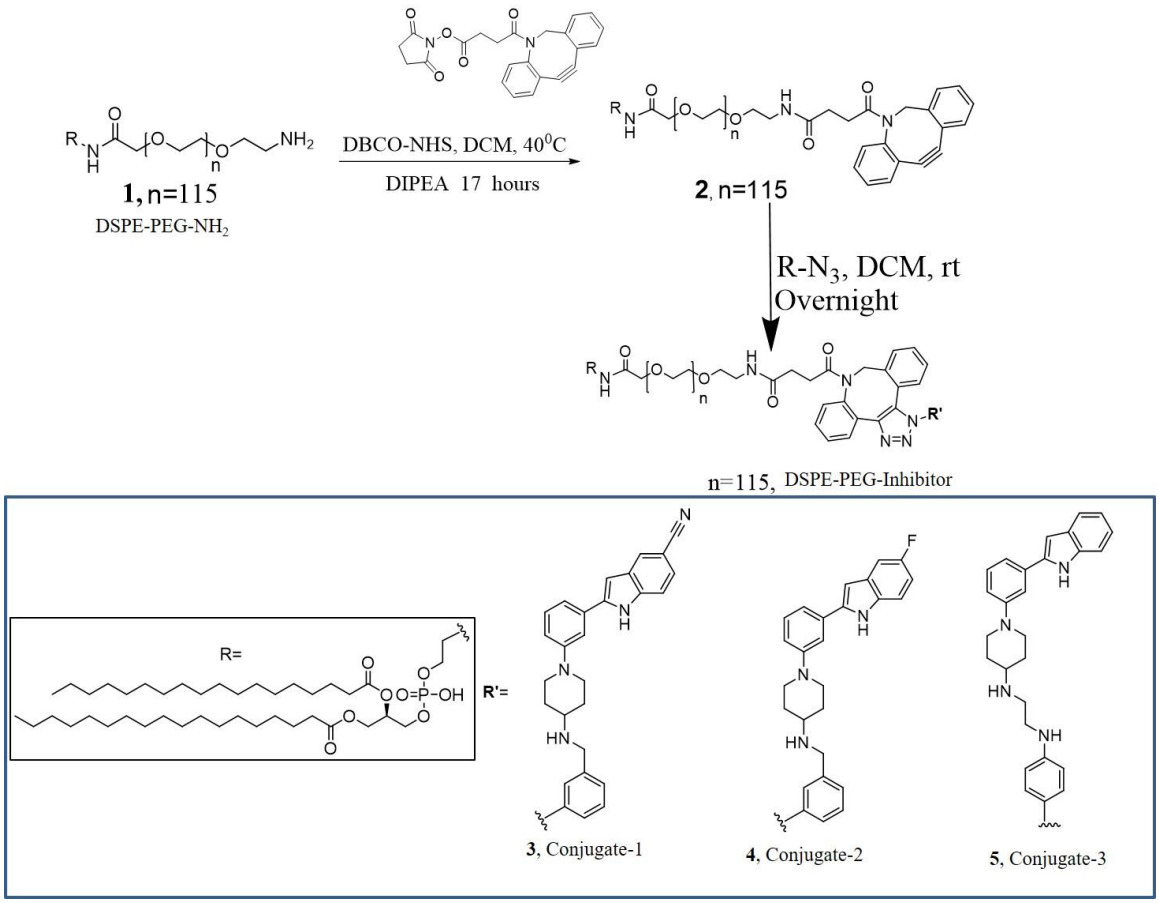

Figure 4: Reaction scheme for synthesis of DSPE-PEG(5k)-Inhibitor conjugates

1,2-distearoyl-*sn*-glycero-3-phosphoethanolamin-polyethylene glycol (5000)-dibenzocyclooctyne (DSPE-PEG5000-DBCO) (2). DSPE-PEG5000-NH_2 (**1**, 50 mg, 0.01 mmol) and NHS-DBCO (20.1 mg, 0.05 mmol) were dissolved in 2 mL of $CHCl_3$ in a 10 mL round bottom flask with a stir bar. DIPEA (18 µL, 0.102 mmol) was added the flask was evacuated and backfilled with N_2. The solution was stirred at 40°C for 17 hours and the reaction progress was monitored by TLC. The volatiles were then removed under reduced pressure and residue purified by silica gel column chromatography using a gradient mobile phase starting with 95:5 DCM:MeOH and increasing in polarity to 80:20 DCM:MeOH to yield **2** as a solid powder. Yield 50%; TLC: R_f =

0.85 (80:20 DCM:MeOH); ^{1}H NMR ($CDCl_3$): δ 0.90 (t, 6H), 1.15- 1.45 (m, 44H), 2.25 (s, 4H), 2.28-2.32 (m, 2H), 2.48-2.53 (m, 2H), 2.75-2.78 (m, 4H), 2.48-3.7 (m, 180H), 3.55-3.60 (m, 400H) 7.40-7.60 (m, 8H).

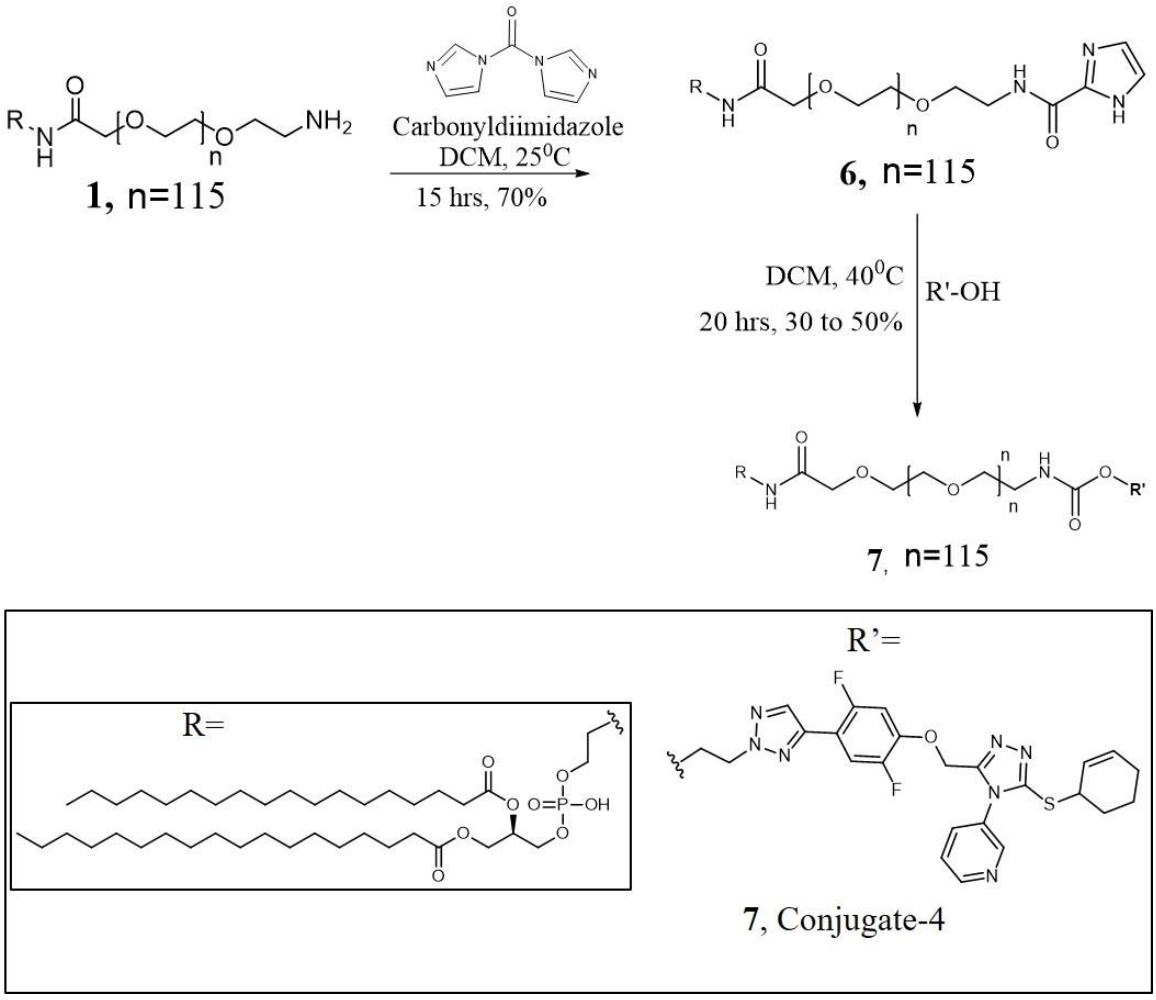

Figure 5: Reaction scheme of conjugate-4 synthesis utilizing CDI coupling

5-Cyanoindole Conjugate-1 (3). DSPE-PEG5000-DBCO (**2**, 10 mg, 0.0023 mmol) and 5-cyanoindole-based Inhibitor-1 (2 mg, 0.0044 mmol) were dissolved in 200 µL DCM in a 1 mL flask. The solution was stirred at room temperature for overnight and the reaction progress was monitored by TLC. The resulting solution was dried in vacuo and residue purified by silica gel

column chromatography using a gradient mobile phase starting with 90:10 DCM: MeOH and increasing in polarity to 83:17 DCM:MeOH. Yield, 25%; TLC: R_f = 0.80 (80:20 DCM:MeOH); ^{1}H NMR ($CDCl_3$): δ 0.90 (t, 6H), 1.15- 1.45 (m, 44H), 2.25 (s, 4H), 2.28-2.32 (m, 2H), 2.48-2.53 (m, 2H), 2.75-2.78 (m, 4H), 2.48-3.7 (m, 180H), 3.55-3.60(m, 400H) 7.40-7.60 (m, 8H)

5-Fluoroindole Conjugate-2 (4). DSPE-PEG5000-DBCO (**2**, 10 mg, 0.0023 mmol) and Inhibitor-2 (2.0 mg, 0.0045 mmol) were dissolved in 200 µL DCM in a 1 mL flask. The solution was stirred at room temperature for overnight and the reaction progress was monitored by TLC. The resulting solution was dried in vacuo and the residue purified by silica gel column chromatography using a gradient mobile phase starting with 90:10 DCM: MeOH and increasing in polarity to 83:17 DCM: MeOH. Yield, 20%; TLC: R_f = 0.80 (80:20 DCM:MeOH); ^{1}H NMR ($CDCl_3$): δ 0.90 (t, 6H), 1.15-1.45 (m, 44H), 2.25 (s, 4H), 2.28-2.32 (m, 2H), 2.48-2.53 (m, 2H), 2.75-2.78 (m, 4H), 2.48-3.7 (m, 180H), 3.55-3.60(m, 400H) 7.40-7.60 (m, 8H).

Indole Conjugate-3 (5). DSPE-PEG5000-DBCO (**2**, 10 mg, 0.0023 mmol) and Inhibitor-3 (2 mg, 0.0044 mmol) were dissolved in 200 µL DCM in a 1 mL flask. The solution was stirred at room temperature for overnight and the reaction progress was monitored by TLC. The resulting solution was dried in vacuo and the residue purified by silica gel column chromatography using a gradient mobile phase starting with 90:10 DCM: MeOH and increasing in polarity to 83:17 DCM: MeOH. Yield, 25%; TLC: R_f = 0.80 (80:20 DCM: MeOH); ^{1}H NMR ($CDCl_3$): δ 0.90 (t, 6H), 1.15- 1.45 (m, 44H), 2.25 (s, 4H), 2.28-2.32 (m, 2H), 2.48-2.53 (m, 2H), 2.75-2.78 (m, 4H), 2.48-3.7 (m, 180H), 3.55-3.60 (m, 400H) 7.40-7.60 (m, 8H).

Triazole Conjugate-4 (7). DSPE-PEG5000-NH_2 (**2**, 100 mg, 0.024 mmol) and carbonyldiimidazole (4 mg, 0.120 mmol) were mixed together in 500 µL DCM in a 2mL flask. The solution was stirred at room temperature for 15 hours to yield 70% of the DSPE-PEG(5k)-

imidazole conjugate. Then, DSPE-PEG(5k)-imidazole (13.31 mg, 0.0038 mmol) and Inhibitor-4 (2 mg, 0.0018 mmol) were mixed in DCM and stirred at 40°C overnight while monitoring the reaction progress by TLC. The resulting solution was dried in vacuo and the residue purified by silica gel column chromatography using a gradient mobile phase starting with 90:10 DCM: MeOH and increasing in polarity to 83:17 DCM: MeOH. Yield, 28%; TLC: R_f = 0.80 (80: 20 DCM:MeOH); ^{1}H NMR ($CDCl_3$): δ 0.90 (t, 6H), 1.15- 1.45 (m, 44H), 2.25 (s, 4H), 2.28-2.32 (m, 2H), 2.48-2.53 (m, 2H), 2.75-2.78 (m, 4H), 2.48-3.7 (m, 180H), 3.55-3.60 (m, 400H) 6.5-8.00 (m, 9H).

2.3.2 p97 purification

Deionized water was used to prepare all buffers. A 0.2 μm filter was used to filter all buffers. The p97 plasmid was transformed into *E. coli* Rosetta and purified as described[22]. A single colony was inoculated into 50 mL LB media containing 100 mg/L ampicillin and 15 mg/L chloramphenicol. Inoculation of a 50 mL starter culture into 1L LB media containing 100 mg/L ampicillin was incubated with shaking at 37 °C until the culture produced an OD_{600} of 0.8. (~2.5h). The culture was then cooled to 20°C and induced with 0.4 mM IPTG and the cell harvested after 15 hours. The approximately 6 gm cell pellet from 2L of culture media was suspended in 30 mL lysis buffer (100 mM Tris, pH 7.4, 500 mM KCl, 5 mM $MgCl_2$, 20 mM imidazole, 5% glycerol, 2 mM β-mercaptoethanol, Roche protease inhibitor tablet) and lysed by six 30-second pulses of probe sonication, separated by 2 min intervals.

The lysate was centrifuged at 20,000g for 45 min at 4 °C and the resulting supernatant was loaded onto three Ni-NTA columns (5 mL suspension) pre-equilibrated with wash buffer (50 mL, 50mM HEPES, pH 7.4, 150 mM KCl, 5 mM $MgCl_2$, 20 mM imidazole)) and incubated at 4 °C with rotation for 30 min. The column was then flushed with wash buffer (100 mL) and His_6-tagged p97

was eluted by stepwise application of 10 mL of imidazole elution buffer (50 mM, 100 mM, 150 mM, 200 mM, and 250 mM imidazole in wash buffer step wise). Protein concentrations were determined for each elution. Fractions from the 150, 200 and 250 mM imidazole steps were combined and concentrated with an Amicon Ultra-15 centrifugal filter unit (NMWL = 100 kDa). The mixture (1 mL of 20 mg/mL) was then fractionated with a gel filtration column (Superdex™ 200), eluted with GF buffer (20 mM HEPES, pH 7.4, 250 mM KCl, 1mM $MgCl_2$) at 0.5 mL/min flow rate, and fractions corresponding to 550 kDa were collected. p97 was exchanged into storage buffer (20 mM HEPES, pH 7.4, 250 mM KCl, 1mM $MgCl_2$, 5% glycerol), 500 µL of 5 mg/mL p97 was aliquoted, frozen in liquid nitrogen, and stored at -80 ^{o}C.

2.3.3 TEM Grid Graphene Coating Procedure

We have used a pyrene solution to cover the maximum area of the TEM grids with a graphene oxide single layer. A 0.100 mg/ml of 3 µL of a pyrene solution was applied on the dull side of a lacey TEM grid and a 3 µL of 0.1 mg/ml graphene oxide was applied just before the pyrene solution dried out. Then, the grid was incubated for 2 minutes. After this, the dull side of the grid was washed three times and the shiny side was washed one time with a 3 µL droplet of water before drying and storing for lipid monolayer deposition.

2.3.4 Langmuir-Schaefer Lipid Monolayer Film Deposition on TEM Grid Surface

A stock solution of fluid phase lipid mixture composed of DSPE-PEG(5k)-inhibitor: mPEG750-DSPE (1:99 mol%) was made in $CHCl_3$ at 1.0 mg/mL and stored at - 80 °C. A 5-8 µL aliquot of the lipid mixture was spread at the air-water interface and compressed into their solid condensed phase to a final surface pressure of 45 mN/m using a Langmuir trough. The condensed monolayer was then deposited via Langmuir-Schafer transfer onto the TEM grid surface (Ted Pella) for subsequent affinity capture of p97 (Figure 1).

2.3.5 Negative Stain Procedure for Immobilized Protein Targets

A 0.100 mg/mL sample of p97 protein was applied to the grid surface, the sample incubated for 10-15 minutes, and then the grids were washed 5 times with 15 µL Tris buffer. A 3-5 µL drop of 1 % uranyl acetate was applied to the grid and incubated for at least 1 minute, then the excess solution removed using the edge of a filter paper wedge and then grid was completely dried under vacuum for 1 hour. Negatively stained images were recorded using a Tecnai T20 transmission electron microscope operating at 200 kV.

2.3.6 Frozen Hydrated Samples Preparation for Cryo-EM

TEM grids surface functionalized with DSPE-PEG(5k)-inhibitor:mPEG750-DSPE (1:99 mol%) monolayers were treated with 0.100 mg/mL of pure p97 and sequentially washed after incubation as described above for negative staining. A final drop of 3 µL of buffer on the grid surface was blotted for 8 seconds at 75-80 % humidity using a Cryoplunger-3 (FEI Company). The grids were plunged into liquid ethane for cryo-fixation and imaged at 200 kV on a TALOS FC200 transmission electron microscope using low-dose techniques. The FEI CCD camera in the Talos was used to record images.

2.3.7 Image processing

All raw movies were aligned and dose-weighted with the latest version of *MotionCor2*. From 625 summed movies, a total of 77,783 particles were picked after carefully going through automated particle picking from *Gautomatch*. Particles were then extracted in *RELION v3.0-beta* before 2-D reference-free classification in *cryoSPARC v2.5*. Results of 2-D classification indicated two different particle states of the recombinant form of human p97; 1) single-ring (hexamer) and 2) double-ring (dodecamer). The *ab initio* model for each particle state were built and subjected to heterogeneous refinement, followed by homogenous refinement in *cryoSPARC v2.5*. A total of

22,225 and 25,029 particles were used for the final 3-D reconstruction of the hexamer and dodecamer particle states, respectively. To improve the resolution, each structure was subjected to per-particle CTF-refinement, beam tilt correction, and Bayesian polishing, followed by 3-D refinement in *RELION v3.0-beta*. The resolution for each particle state was further improved using an in-house developed version of *jspr.py*. need to fix this

2.4 Performance of Inhibitor Modified TEM-Grid by TEM and Cryo-EM Analysis

Micrographs obtained from TEM analysis revealed disclosed that there are very few p97 particles particles adsorbed onto bare grids and mPEG750 modified grids after 5 washes (Figure 6F). Our data shows that the particle distribution on bare grids is almost the same as DSPE-mPEG750 functionalized grids which were used as control (Figure 4A-D). Based on these findings we conclude that the brush regime of DSPE-PEG750 monolayers deposited on to the grid surface by LS transfer are an effective means to avoid non-specific adsorption of p97 onto TEM grid surfaces. Purified p97 (0.100 mg/mL) was used in this non-specific adsorption experiment. Grids coated with mPEG750-DSPE monolayers showed a greatly reduced accumulation of p97 (Figure 6E, 6F). The low abundance of p97 particles in this image highlights the antifouling properties of these PEGylated surfaces. We infer from these findings that the non-fouling properties of the mPEG750-DSPE brush monolayer makes it a good matrix for limiting non-specific adsorption onto inhibitor modified grids.

Next, we sought to assess direct affinity guided interactions with inhibitor modified grids after evaluating nonspecific adsorption of p97. First, we used a TECNAI-T20 microscope to monitor p97 capture on grids bearing 1:99 and 3:97 mol% inhibitor : mPEG750 lipid monolayers. A stock solution of $CHCl_3$ containing 99% mPEG750-DSPE and 1 % DSPE-PEG(5k)-Inhibitor were

spread at air-water interface at room temperature. An incubation period of 5 minutes was used to evaporation of $CHCl_3$ from the Langmuir trough water surface. The pressure-area isotherms for a 1:99 molar ratio of DSPE-PEG5000-Inhibitor:mPEG750-DSPE mixtures showed progressively increasing surface pressures upon monolayer compression. We explain this observation such that as the compression process proceeds, the lipid monolayer film reaches the brush regime at 45 mN/m from the initial mushroom regime. The 400 mesh TEM grid surface functionalized with lipid film can be stored in room temperature for few months. The grids stained with 1% $UO_2(OAc)_2$ revealed that 3% DSPE-PEG-inhibitor modified grid contained a higher density of p97 than 1% DSPE-PEG-inhibitor modified grids (Figure 8A and 8B). We infer from these negatively stained images that sufficiently large areas of the grids were covered with stabilized mixed monolayer (Figure 8A and 8B). Furthermore, it was observed be seen that there are still large areas of the grids that are covered with p97 after 5 washes of buffer (Figure 7A, 7B, 7D and 7E), indicating that the affinity for p97 was strong and specific since nonspecific interactions of p97 with the DSPE-mPEG750 surface were displaceable by extensive washing. Bare grids without protein (Figure 6A), with 0.100 mg/mL protein including without washes (Figure 6B), 2 times and 5 times washed showed minimal p97 particle in the images (Figure 6C and 6D). TEM grids functionalized with 100 %

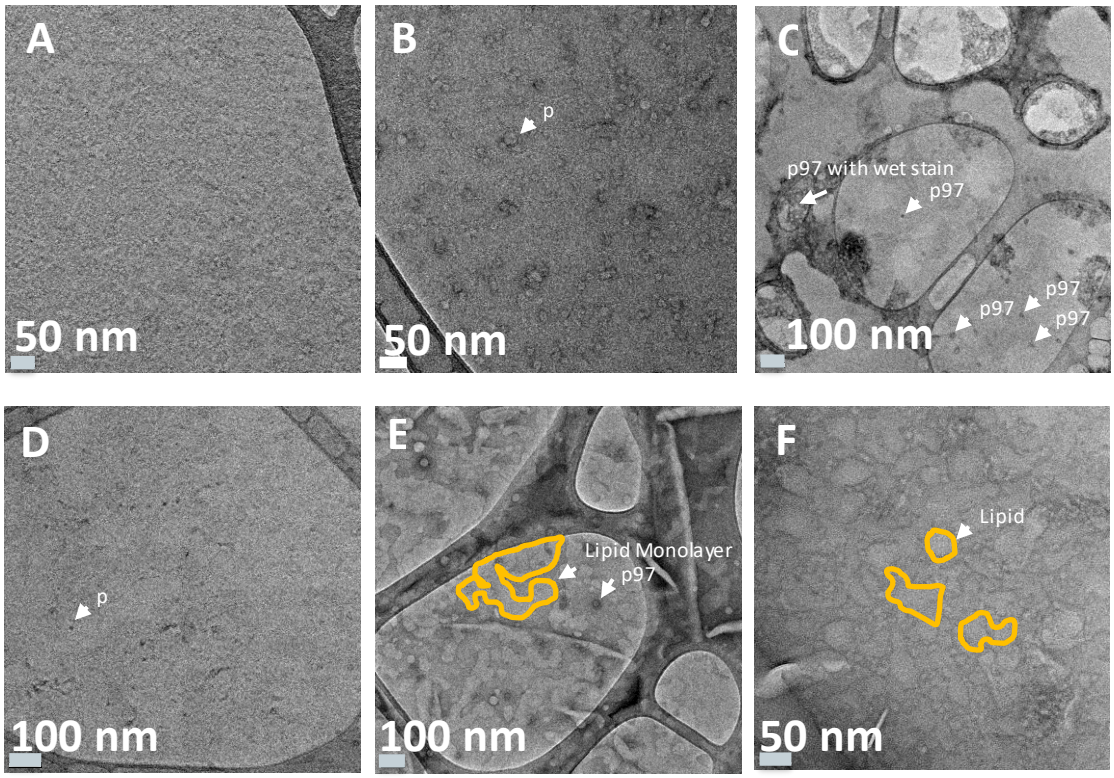

Figure 6: Characterization of non-fouling properties of DSPE-mPEG750.
A) Bare grid, No protein, B) without wash Bare grid, 0.100 mg/ml p97, C) 2 times washed Bare grid, and 0.100 mg/ml D) bare grid and 0.100 mg/ml, 5 times washed E) Only mPEG750-DSPE grid, 0.100 mg/ml, 2 times washed and F) Only mPEG750-DSPE grid, 0.100 mg/ml, 5 times washed.

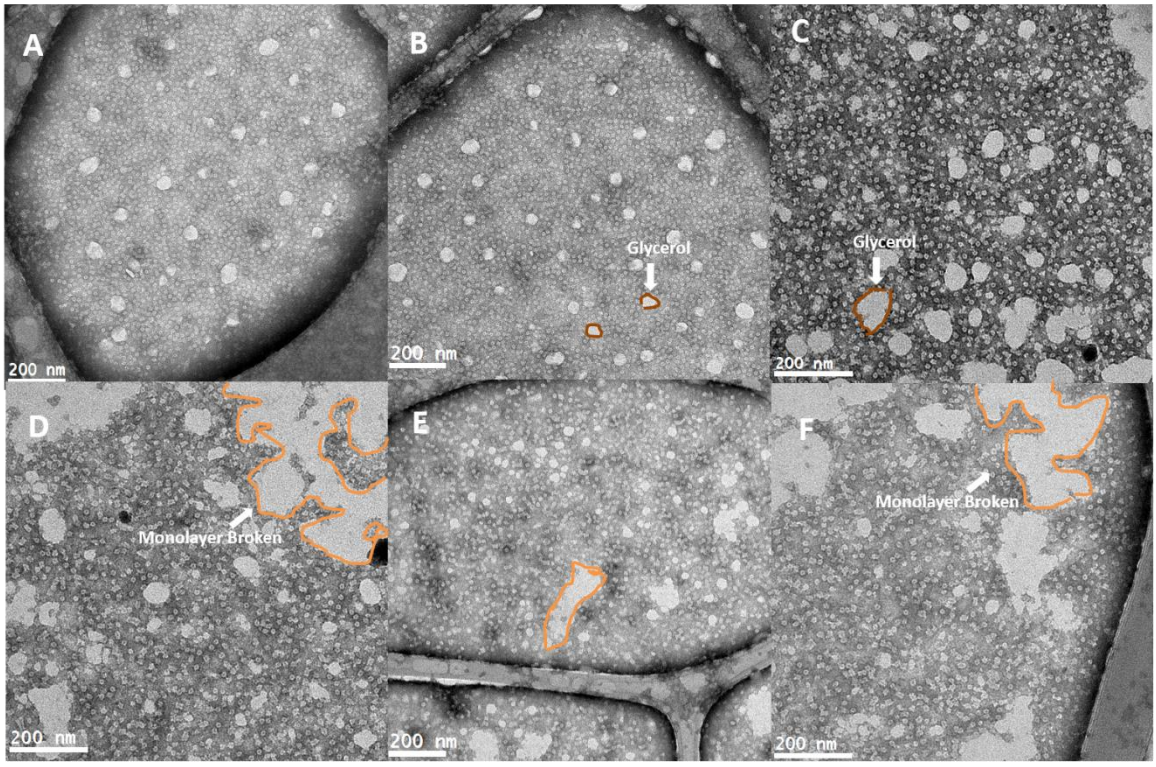

Figure 7: Characterization of negative stained p97 captured by partial DSPE-PEG-Inhibitor-1 from different concentration of target particle. Negative stained p97 captured by 1 % DSPE-PEG-Inhibitor-1 from 300 µg/ml (A), 200 µg/ml (B), 100 µg/ml, D) 75 µg/ml, (E) 40 µg/ml, F) 15 µg/ml concentration

mPEG750-DSPE including 0.100 mg/ml plus 5 times washed (Figure 6E)

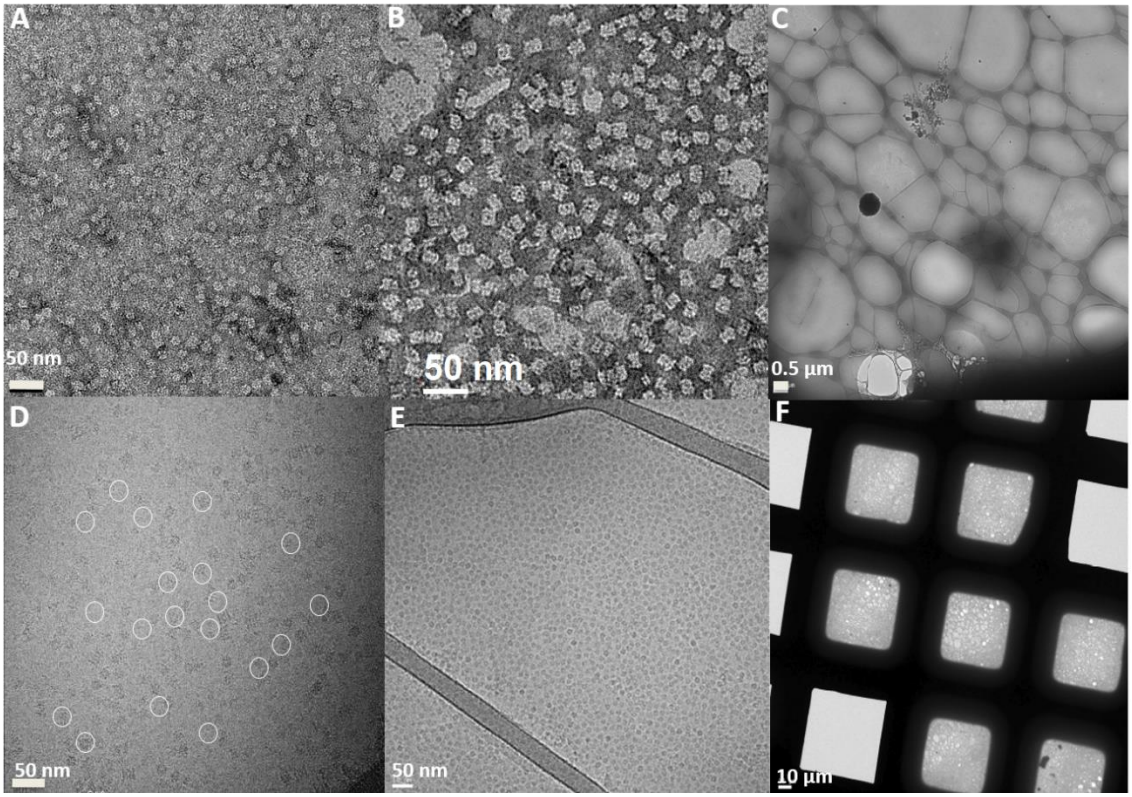

Figure 8: Characterization of negative stained p97 captured by different partial DSPE-PEG-Inhibitor-1. Negative stained p97 captured by 1 % DSPE-PEG-Inhibitor-1(A), 3 % DSPE-PEG-Inhibitor-1 (B), 2C) Low magnification micrograph of 1 % DSPE-PEG-Inhibitor-1 grid in titan, D) Cryo EM micrograph of p97 of 1 % DSPE-PEG-Inhibitor-1, (E) and F) Low magnification image of 1 % inhibitor modified TEM grid in Cryo-EM.

showed much fewer particles than 2 times washed, further indicating nonspecific interaction of p97 with the grid surface. p97 captured on grids bearing 1:99 and 3:97 mol% DSPE-PEG5000-Inhibitor-1:mPEG750-DSPE monolayers were clearly demonstrated by TEM (Figure **7**). Micrographs from grids revealed a uniform, concentration-dependent p97 distribution on the surface (Figure 7A-F). These findings indicate that p97 targets can be captured in an Inhibitor concentration-dependent manner, with higher Inhibitor loadings (3 mol%) producing greater target protein concentrations (Figure 7B) than 1% loadings on the grid (Figure 7A). We also have

observed that 1% DSPE-PEG5000-Inhibitor-1 monolayers can detect p97 from less than 15 µg/ml concentration (Figure 7F).

2.5 Results and Discussion

Cryo-EM Processing and Assessment.

Particles captured by inhibitor modified lipopolymer were frozen onto graphene coated lacey carbon EM grids. Samples were examined with a Titan Krios electron microscope (FEI). A cryo-EM dataset generated a dodecamer map of p97 with a resolution of 3.64 Å (Figure 11 B, D) and hexamer map 4.33 Å (Figure 11 A, C) based on the "gold-standard" Fourier shell correlation (FSC) using the FSC = 0.143 criterion. We compared our p97 3.64 Å resolution cryo-EM map with published p97 2.3 Å resolution[23] to verify accuracy using D6 symmetry.

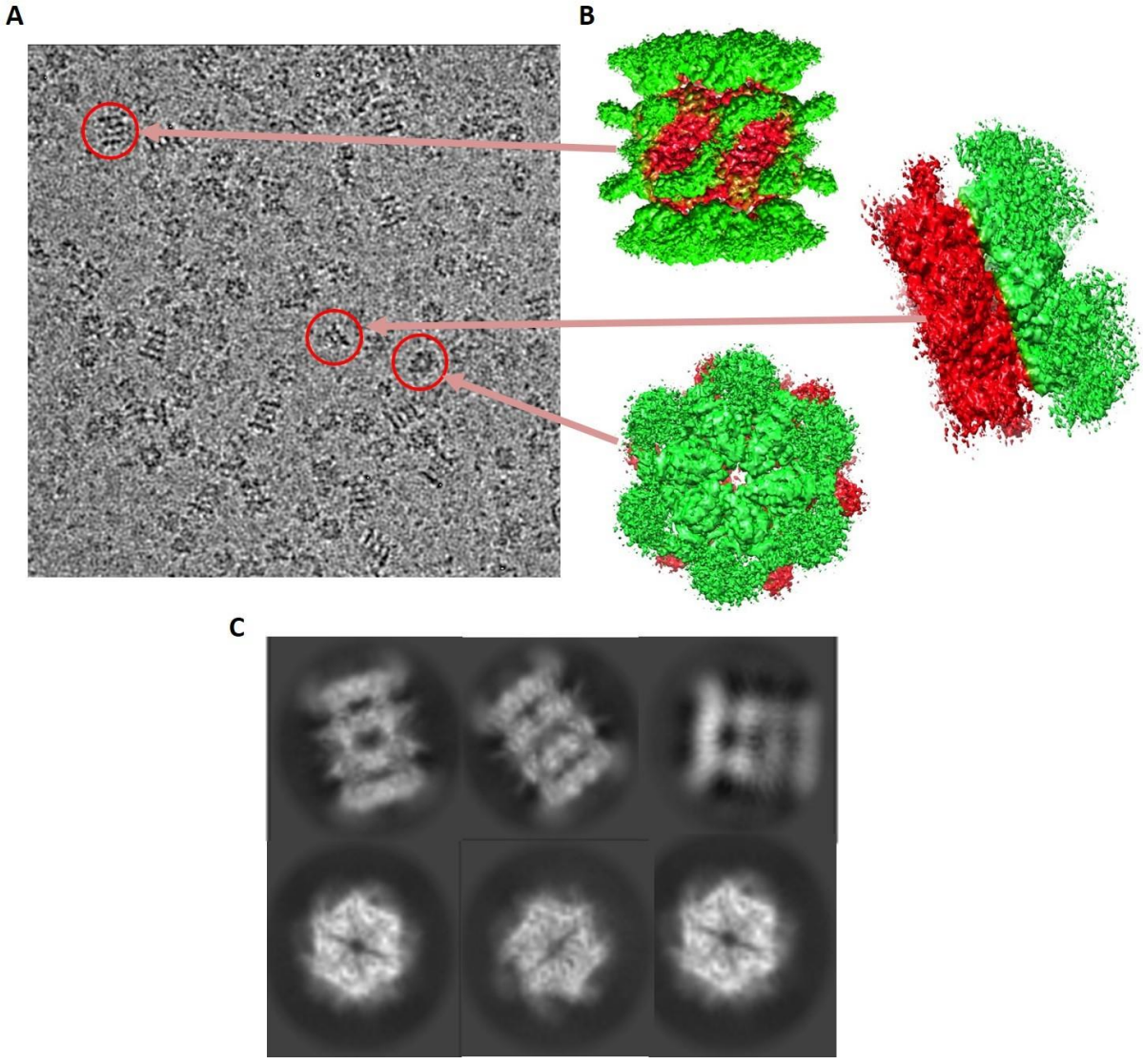

Figure 9: Intermediate stages in structure determination of wild-type p97. A) and B) displaying p97 homohexamers and dodecamer in different orientations corresponding to our resolved density map; C) 2D class averages showing that both top and side views of dodecamer map of p97.

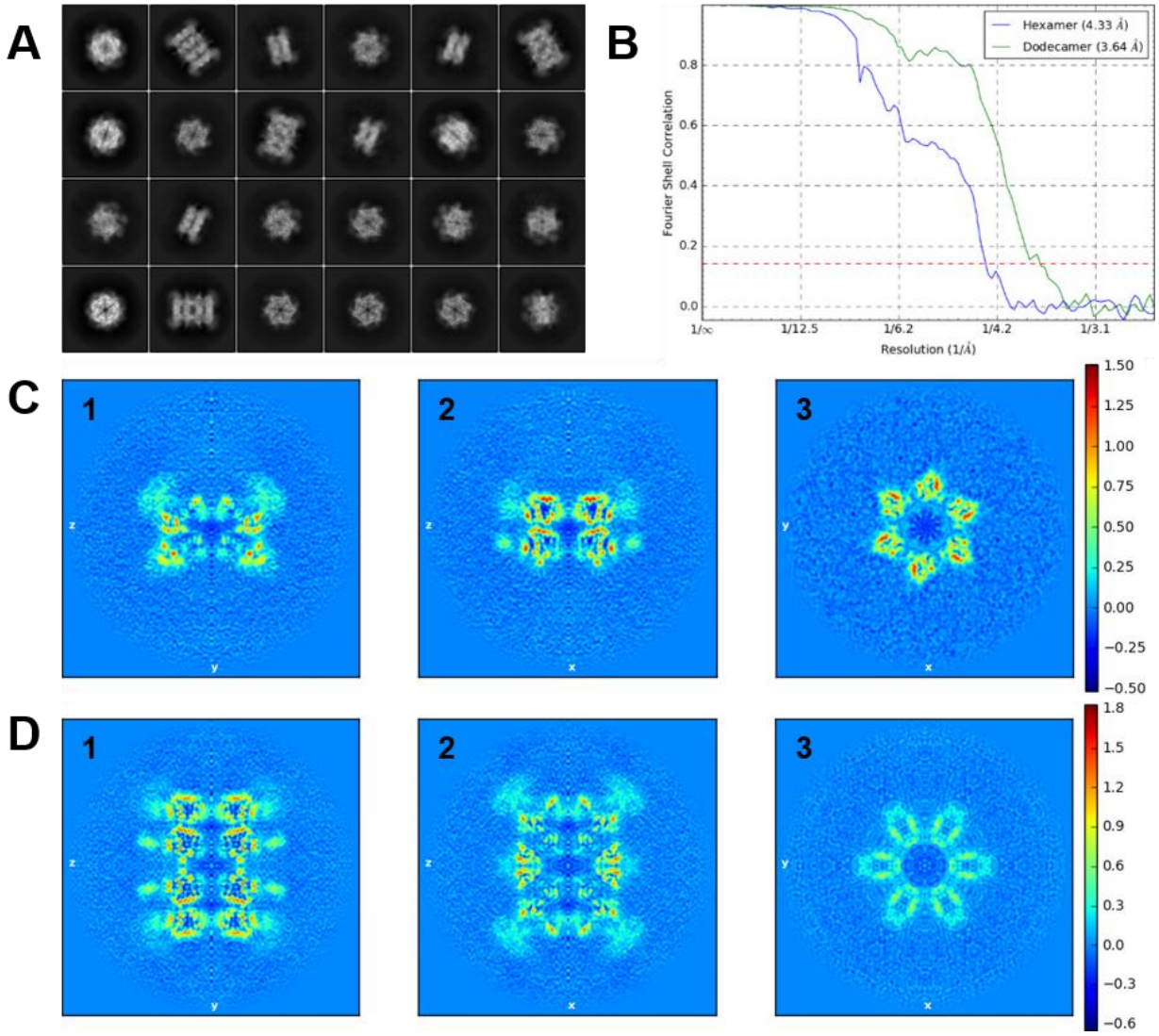

Figure 10: Image processing of p97. (A) Reference-free 2-D classes averages showing different views of both hexamer and dodecamer states represented in the data. (B) Fourier Shell Correlation (FSC) plots. Shown in blue and green is the FSC curve between two independently refined halves of the hexamer and dodecamer states, respectively. The dashed-line (red) represents the gold-standard FSC=0.143 criterion. The X (1), Y (2), and Z (3) axes views are shown for the (C) hexamer and (D) dodecamer p97 states.

As compare to 2.3 Å resolution of p97 map[23], we found substantial difference in our density map. We infer from our findings that the electron density map at 3.64 Å resolution reveals the two p97 homo-hexamers are linked through D1 domains which are very similar to p97 model when it is

stacked together through the D1 domains (Figure 12 D and resolution for N domain has been lost (Figure 12 A, B). We have found six different densities around D1 domain around D1 domain.

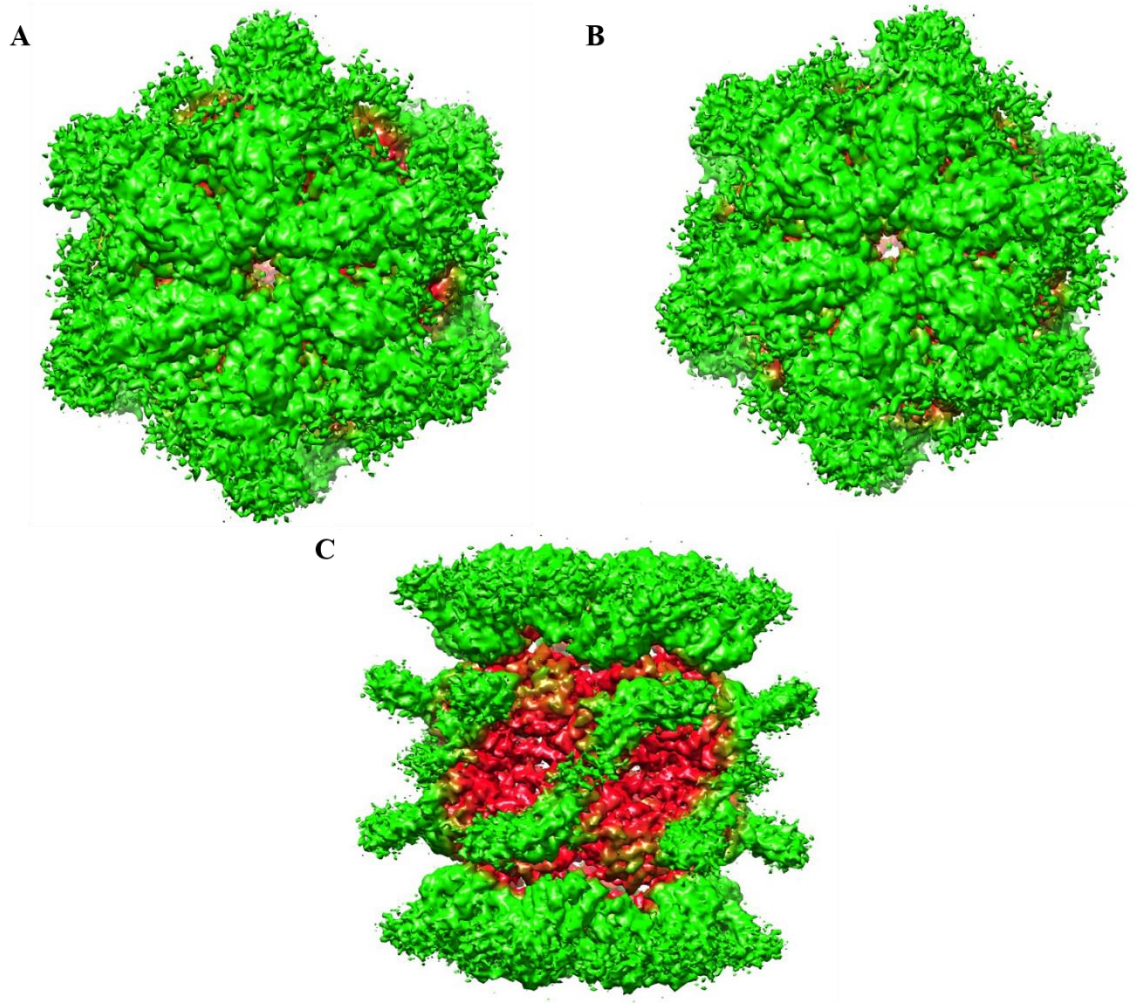

Figure 11: 3.64 Å Resolution density map of p97 A) Top View, B) Bottom view and, C) Side view

As expected, we used a long PEG spacer to avoid potential preferred orientations of p97 that may occur if the tether length between the protein and surface is too short. We infer from our finding that inhibitor modified lipid coated TEM grid specifically capture p97 with different orientation for conformational change (Figure 10 A-B). We further analyzed the structure to find out newly found densities and how inhibitor binds between the domains. Additional structure (electron

density) information seen in our cryo-EM maps vs. Subramaniam map(s) and comparison to other known structures of p97 shown in figure-14. The structural intermediates of p97 are shown in figure 15. We also reconstructed homo-hexamer of p97 by masking one ring of dodecamer at 4.33 Å which looks identical to the density map resolved at 2.3 Å. The implication of this differences is not clear at this time. The key interaction of indole derivative part wasn't resolved for low resolution different domain junctions.

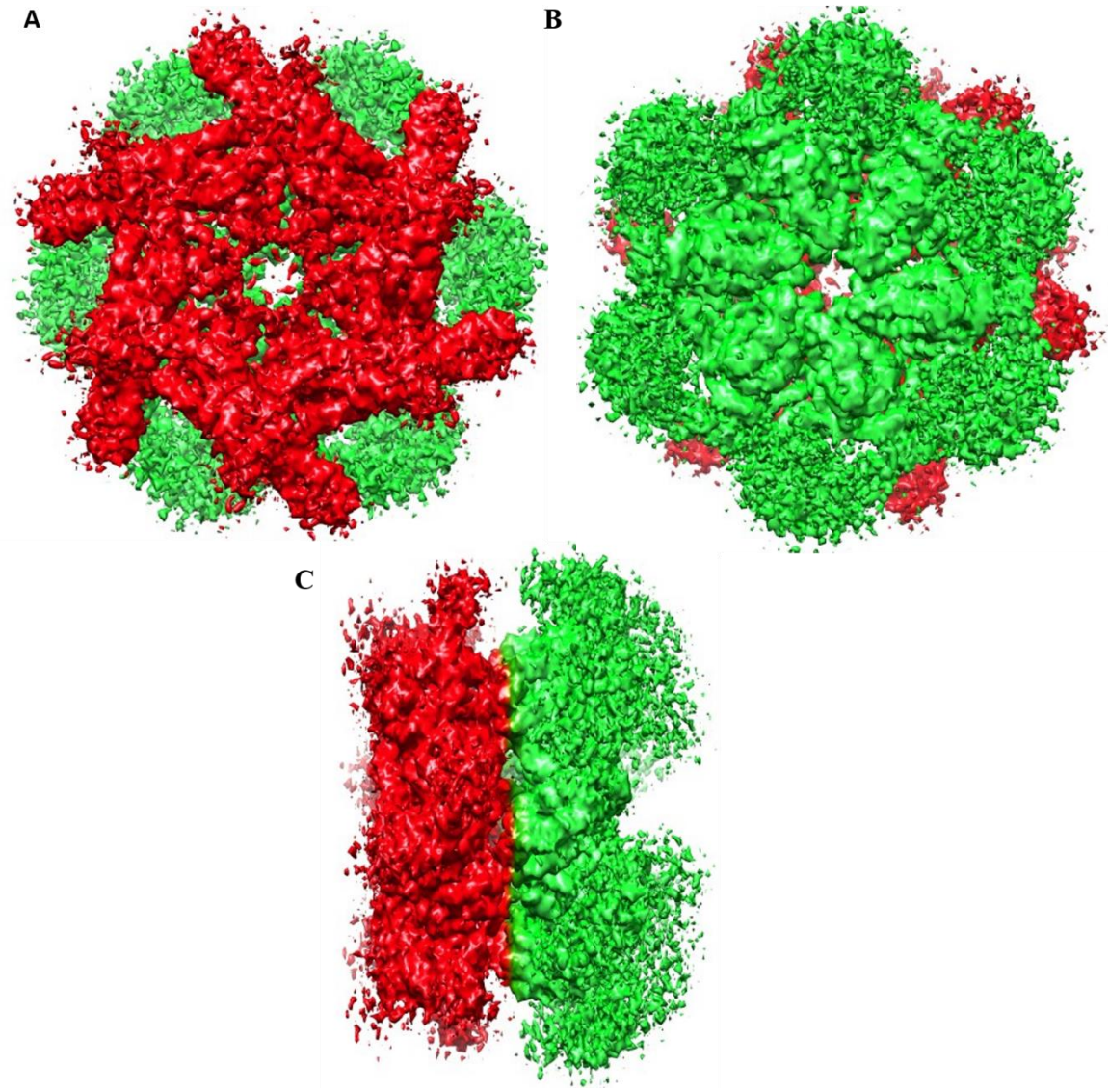

Figure 12: 4.33 Å Resolution density map of hexamer p97, A) Top View, B) Bottom view and, C) Side view

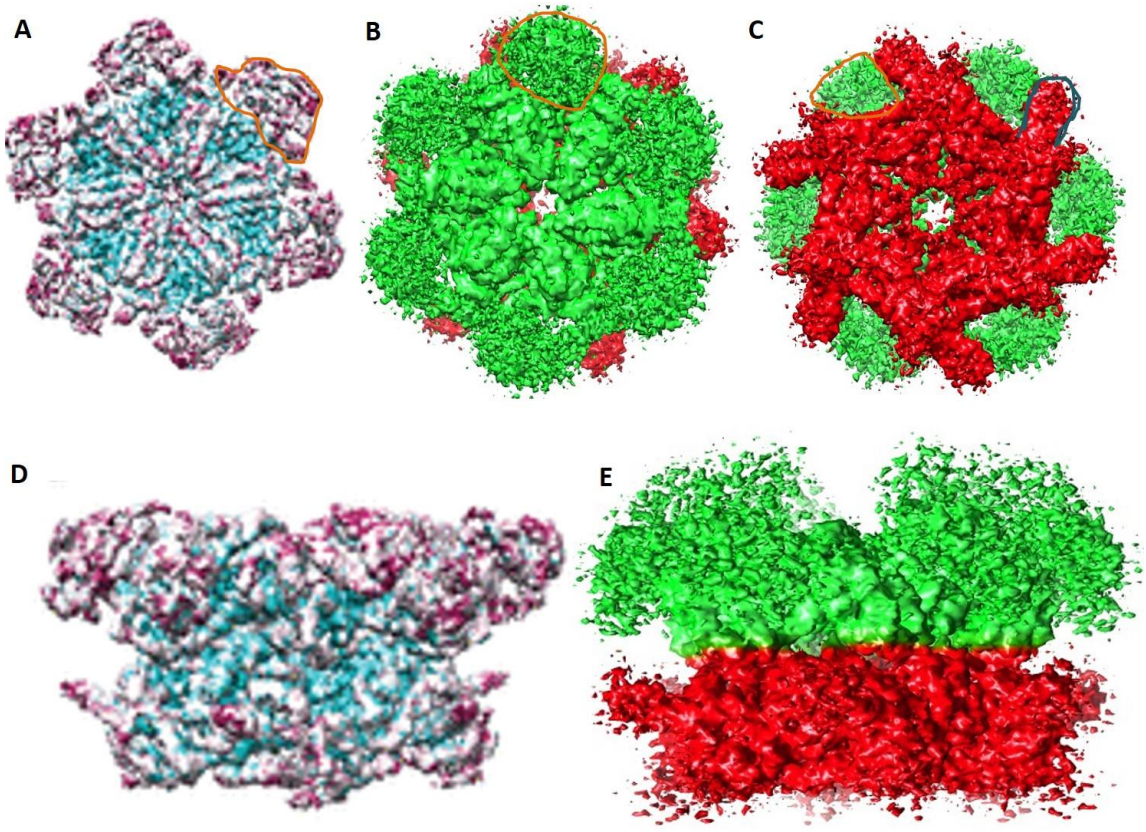

Figure 13: Comparative density map of p97 at 2.3 Å and 4.33 Å. Marked by orange color shows N domain (marked) in A) top view at 2.3 Å reconstructed by Subrahamium et al, B) top, C) bottom view, dark green shows extra density. D) side view at 2.3 Å and E) at 4.33 Å resolution of p97.

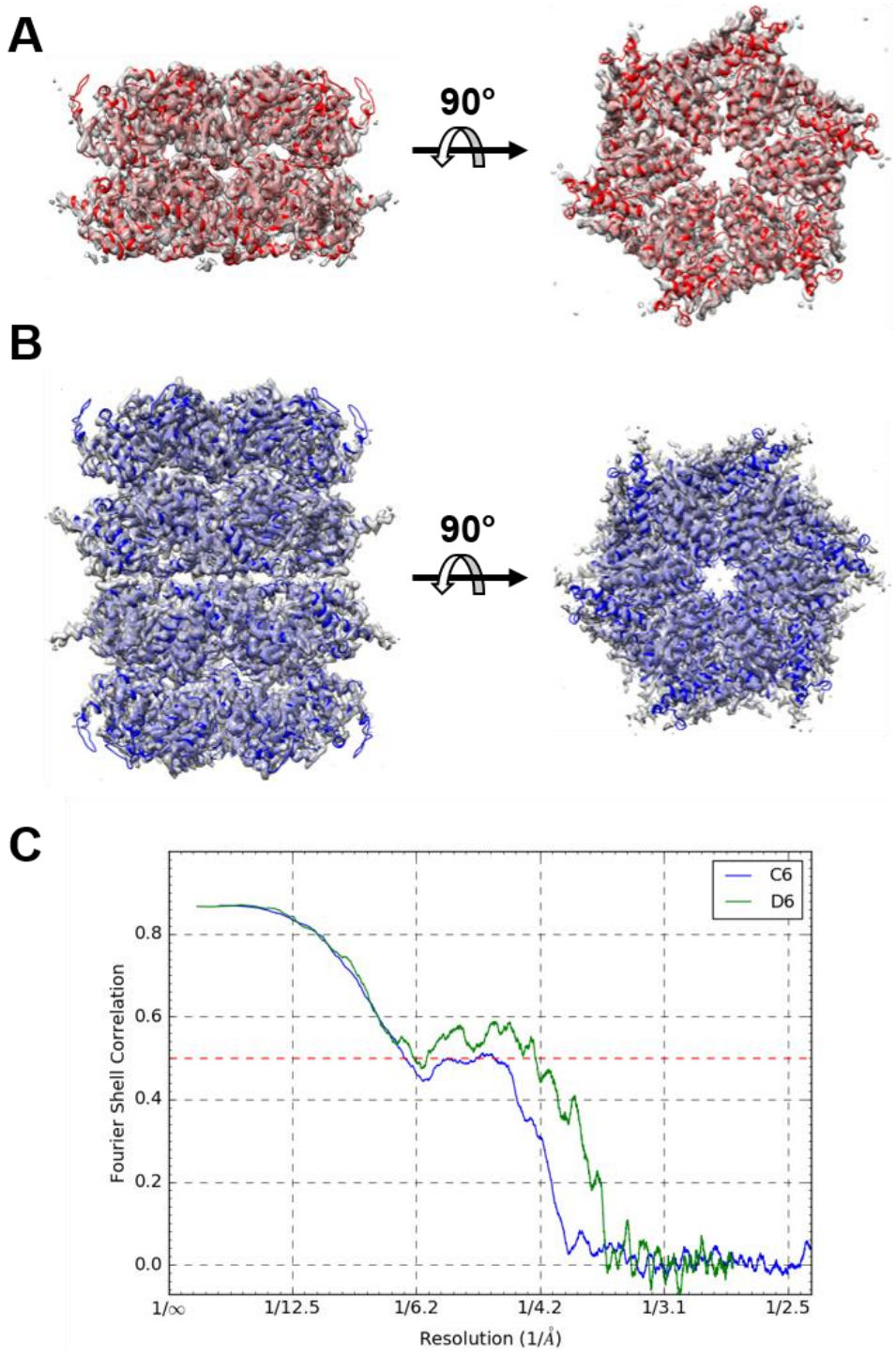

Figure 14 Additional structure (electron density) information seen in our cryo-EM maps vs. Subramaniam map(s) and comparison to other known structures of p97. Top/bottom and side views of (A) C6 and (B) D6 structure states. (C) Model-map FSC curves of each structur

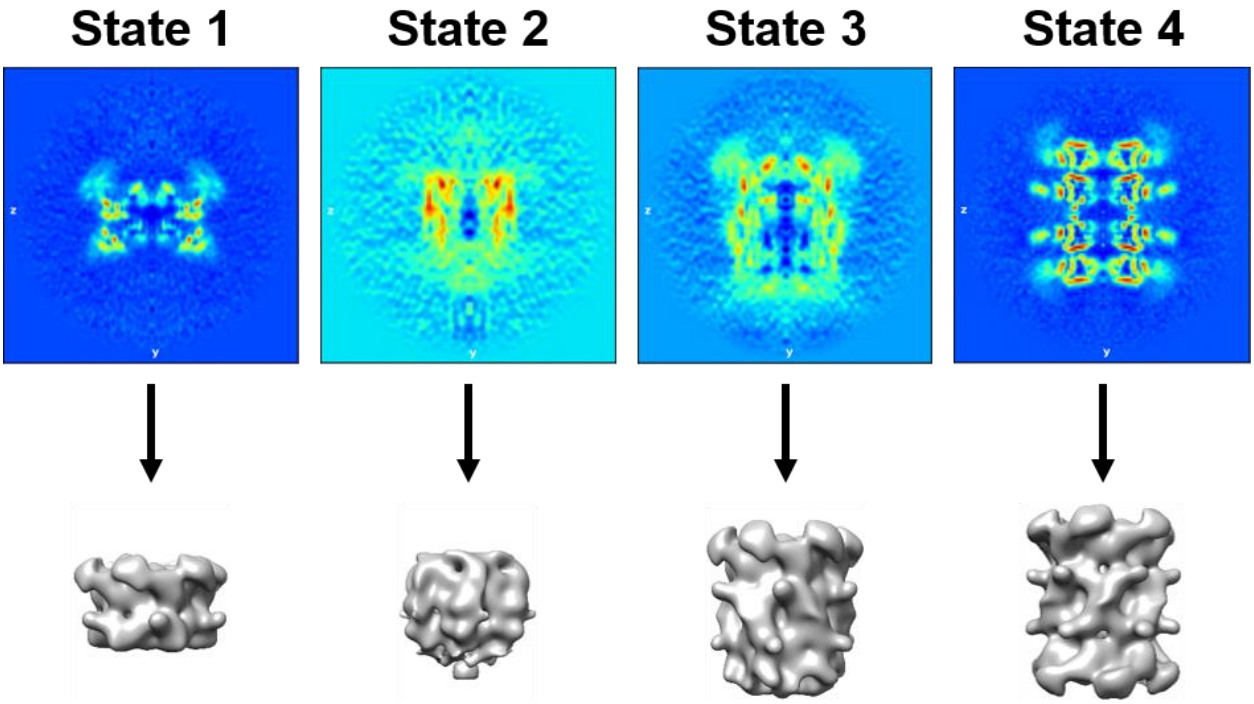

Figure 15 Structural intermediate states of p97.

2.6 Conclusions

A library of inhibitor-modified lipopolymers was made where PEG was conjugated to a lipid anchor and an inhibitor for use as an affinity ligand. We have synthesized four drug conjugates composed of a flexible water-soluble polyethylene glycol 5000 unit attached to 1,2-distearoyl-*sn*-glycero-3-phosphoethanolamine at one end of the polymer and four different drug candidates at the other end of the polymer to provide a high affinity interaction with p97 and concentrate it at the grid surface. Our inhibitor modified affinity approach was performed to work for capturing non-engineered proteins as expected. A long PEG spacer is used in this case to avoid potential preferred orientations of p97 that may occur if the tether length between the protein and surface is too short.

As mPEG750-DSPE was shown to work as a non-fouling surface to avoid nonspecific adsorption of p97, we used 1 mol% of DSPE-PEG(5k)-Inhibitor in an mPEG750-DSPE matrix to avoid

protein aggregation. We anticipate that this inhibitor modified affinity approach can be used to capture any target particle from cell lysates using ligands with high affinity for the desired protein target.

2.7 Acknowledgements

A p97 plasmid for single particle cryo-EM analysis was a gift provided by Tsui-Fen Chou at University of California, Los Angeles. A library of well characterized p97 inhibitors was provided by the Wipf and Huryn Groups at the University Pittsburgh.

2.8 References

1. Benjamin, C. J.; Wright, K. J.; Hyun, S.-H.; Krynski, K.; Yu, G.; Bajaj, R.; Guo, F.; Stauffacher, C. V.; Jiang, W.; Thompson, D. H., Nonfouling NTA-PEG-Based TEM Grid Coatings for Selective Capture of Histidine-Tagged Protein Targets from Cell Lysates. *Langmuir* **2016,** *32* (2), 551-559.

2. Kelly, D. F.; Abeyrathne, P. D.; Dukovski, D.; Walz, T., The Affinity Grid: a pre-fabricated EM grid for monolayer purification. *Journal of molecular biology* **2008,** *382* (2), 423-433.

3. Kelly, D. F.; Dukovski, D.; Walz, T., Strategy for the use of affinity grids to prepare non-His-tagged macromolecular complexes for single-particle electron microscopy. *Journal of molecular biology* **2010,** *400* (4), 675-681.

4. Yu, G.; Li, K.; Jiang, W., Antibody-based affinity cryo-EM grid. *Methods (San Diego, Calif.)* **2016,** *100*, 16-24.

5. Valle, C. W.; Min, T.; Bodas, M.; Mazur, S.; Begum, S.; Tang, D.; Vij, N., Critical Role of VCP/p97 in the Pathogenesis and Progression of Non-Small Cell Lung Carcinoma. *PLOS ONE* **2011,** *6* (12), e29073.

6. Otter-Nilsson, M.; Hendriks, R.; Pecheur-Huet, E. I.; Hoekstra, D.; Nilsson, T., Cytosolic ATPases, p97 and NSF, are sufficient to mediate rapid membrane fusion. *The EMBO journal* **1999,** *18* (8), 2074-2083.

7. Meyer, H.; Weihl, C. C., The VCP/p97 system at a glance: connecting cellular function to disease pathogenesis. *Journal of Cell Science* **2014,** *127* (18), 3877-3883.

8. Fang, L.; Hemion, C.; Pinho Ferreira Bento, A. C.; Bippes, C. C.; Flammer, J.; Neutzner, A., Mitochondrial function in neuronal cells depends on p97/VCP/Cdc48-mediated quality control. *Frontiers in cellular neuroscience* **2015,** *9*, 16-16.

9. Barthelme, D.; Sauer, R. T., Origin and Functional Evolution of the Cdc48/p97/VCP AAA+ Protein Unfolding and Remodeling Machine. *Journal of Molecular Biology* **2016,** *428* (9, Part B), 1861-1869.

10. Avci, D.; Lemberg, M. K., Clipping or Extracting: Two Ways to Membrane Protein Degradation. *Trends in Cell Biology* **2015,** *25* (10), 611-622.

11. Yi, P.; Higa, A.; Taouji, S.; Bexiga, M. G.; Marza, E.; Arma, D.; Castain, C.; Le Bail, B.; Simpson, J.; Rosenbaum, J.; Balabaud, C.; Bioulac-Sage, P.; Blanc, J.-F.; Chevet, E., Sorafenib-mediated targeting of the AAA+ ATPase p97/VCP leads to disruption of the secretory pathway, endoplasmic reticulum stress and hepatocellular cancer cell death. *Molecular Cancer Therapeutics* **2012.**12.Tao, S.; Tillotson, J.; Wijeratne, E. M. K.; Xu, Y.-m.; Kang, M.; Wu, T.; Lau, E. C.; Mesa, C.; Mason, D. J.; Brown, R. V.; La Clair, J. J.; Gunatilaka, A. A. L.; Zhang, D. D.; Chapman, E., Withaferin A Analogs That Target the AAA+ Chaperone p97. *ACS Chemical Biology* **2015,** *10* (8), 1916-1924.

13. Polucci, P.; Magnaghi, P.; Angiolini, M.; Asa, D.; Avanzi, N.; Badari, A.; Bertrand, J.; Casale, E.; Cauteruccio, S.; Cirla, A.; Cozzi, L.; Galvani, A.; Jackson, P. K.; Liu, Y.; Magnuson, S.; Malgesini, B.; Nuvoloni, S.; Orrenius, C.; Sirtori, F. R.; Riceputi, L.; Rizzi, S.; Trucchi, B.; O'Brien, T.; Isacchi, A.; Donati, D.; D'Alessio, R., Alkylsulfanyl-1,2,4-triazoles, a New Class of Allosteric Valosine Containing Protein Inhibitors. Synthesis and Structure–Activity Relationships. *Journal of Medicinal Chemistry* **2013,** *56* (2), 437-450.

14. Magnaghi, P.; D'Alessio, R.; Valsasina, B.; Avanzi, N.; Rizzi, S.; Asa, D.; Gasparri, F.; Cozzi, L.; Cucchi, U.; Orrenius, C.; Polucci, P.; Ballinari, D.; Perrera, C.; Leone, A.; Cervi, G.; Casale, E.; Xiao, Y.; Wong, C.; Anderson, D. J.; Galvani, A.; Donati, D.; O'Brien, T.; Jackson, P. K.; Isacchi, A., Covalent and allosteric inhibitors of the ATPase VCP/p97 induce cancer cell death. *Nature Chemical Biology* **2013,** *9*, 548.

15. Fang, C.-J.; Gui, L.; Zhang, X.; Moen, D. R.; Li, K.; Frankowski, K. J.; Lin, H. J.; Schoenen, F. J.; Chou, T.-F., Evaluating p97 Inhibitor Analogues for Their Domain Selectivity and Potency against the p97–p47 Complex. *ChemMedChem* **2015,** *10* (1), 52-56.

16. Chou, T.-F.; Li, K.; Frankowski, K. J.; Schoenen, F. J.; Deshaies, R. J., Structure–Activity Relationship Study Reveals ML240 and ML241 as Potent and Selective Inhibitors of p97 ATPase. *ChemMedChem* **2013,** *8* (2), 297-312.

17. Chou, T.-F.; Deshaies, R. J., Development of p97 AAA ATPase inhibitors. *Autophagy* **2011,** *7* (9), 1091-1092.

18. Chou, T.-F.; Brown, S. J.; Minond, D.; Nordin, B. E.; Li, K.; Jones, A. C.; Chase, P.; Porubsky, P. R.; Stoltz, B. M.; Schoenen, F. J.; Patricelli, M. P.; Hodder, P.; Rosen, H.; Deshaies, R. J., Reversible inhibitor of p97, DBeQ, impairs both ubiquitin-dependent and autophagic protein clearance pathways. *Proceedings of the National Academy of Sciences* **2011,** *108* (12), 4834-4839.

19. Chapman, E.; Maksim, N.; de la Cruz, F.; La Clair, J., Inhibitors of the AAA+ Chaperone p97. *Molecules* **2015,** *20* (2), 3027.

20. Alverez, C.; Arkin, M. R.; Bulfer, S. L.; Colombo, R.; Kovaliov, M.; LaPorte, M. G.; Lim, C.; Liang, M.; Moore, W. J.; Neitz, R. J.; Yan, Y.; Yue, Z.; Huryn, D. M.; Wipf, P., Structure–Activity Study of Bioisosteric Trifluoromethyl and Pentafluorosulfanyl Indole Inhibitors of the AAA ATPase p97. *ACS Medicinal Chemistry Letters* **2015,** *6* (12), 1225-1230.

21. Banerjee, S.; Bartesaghi, A.; Merk, A.; Rao, P.; Bulfer, S. L.; Yan, Y.; Green, N.; Mroczkowski, B.; Neitz, R. J.; Wipf, P.; Falconieri, V.; Deshaies, R. J.; Milne, J. L. S.; Huryn, D.; Arkin, M.; Subramaniam, S., 2.3 Å resolution cryo-EM structure of human p97 and mechanism of allosteric inhibition. *Science* **2016,** *351* (6275), 871-875.

22. Chou, T.-F.; Bulfer, S. L.; Weihl, C. C.; Li, K.; Lis, L. G.; Walters, M. A.; Schoenen, F. J.; Lin, H. J.; Deshaies, R. J.; Arkin, M. R., Specific inhibition of p97/VCP ATPase and kinetic analysis demonstrate interaction between D1 and D2 ATPase domains. *Journal of molecular biology* **2014,** *426* (15), 2886-2899.

23. Banerjee, S.; Bartesaghi, A.; Merk, A.; Rao, P.; Bulfer, S. L.; Yan, Y.; Green, N.; Mroczkowski, B.; Neitz, R. J.; Wipf, P.; Falconieri, V.; Deshaies, R. J.; Milne, J. L.; Huryn, D.; Arkin, M.; Subramaniam, S., 2.3 Å resolution cryo-EM structure of human p97 and mechanism of allosteric inhibition. *Science* **2016,** *351*, 871-875.

CHAPTER 3. POLYROTAXANE-BASED ROD-SHAPED SCAFFOLD APPROACH FOR SINGLE PARTICLE RECONSTRUCTION ANALYSIS

3.1 Project Overview

Single particle reconstruction (SPR) analysis of cryoelectron microscopy (cryoEM) data is a rapidly growing method for determining the near-atomic molecular structures of biological samples[1-4]. The reason behind this growing interest in the SPR technique are greatly reduced demand for sample, the capacity to image large, multi-protein complexes that are embedded within cryofixed samples that are several hundred nanometers thick; and improved safety in instances where the sample is of pathogenic origin. Nonetheless, SPR requires large single particle populations, automated class-averaging methods, and advanced computational approaches to achieve near-atomic resolution.[5-7] Increased sampling is somewhat addressed by microscope automation and direct detection[8-10]. Improvements in sample preparation and reliability are still lacking, however, despite efforts to develop different types of "affinity grids",[11-17] modified graphene,[15, 18] and engineered 2D protein arrays[19].

A big challenge for cryo-EM reconstruction is that the method often needs around 100,000 or more images of the target particle at near atomic resolution. Since, cryo-EM technique requires target biomolecules in the microgram to milligram per milliliter range, this makes data collection a big challenge. Thus, accelerated SPA by cryo-EM highly demands to develop the materials and methods that can provide higher probability of viewing the target particles in the vitrified sample.

Therefore, we develop novel material that concentrates the rare biological sample onto a rod-like scaffold prior to deposition onto the TEM grid and actively discourage non-specific protein

adsorption, while enhancing the capture and random presentation of target proteins on the rod-like scaffold. Overall scheme of project is shown in figure 1.

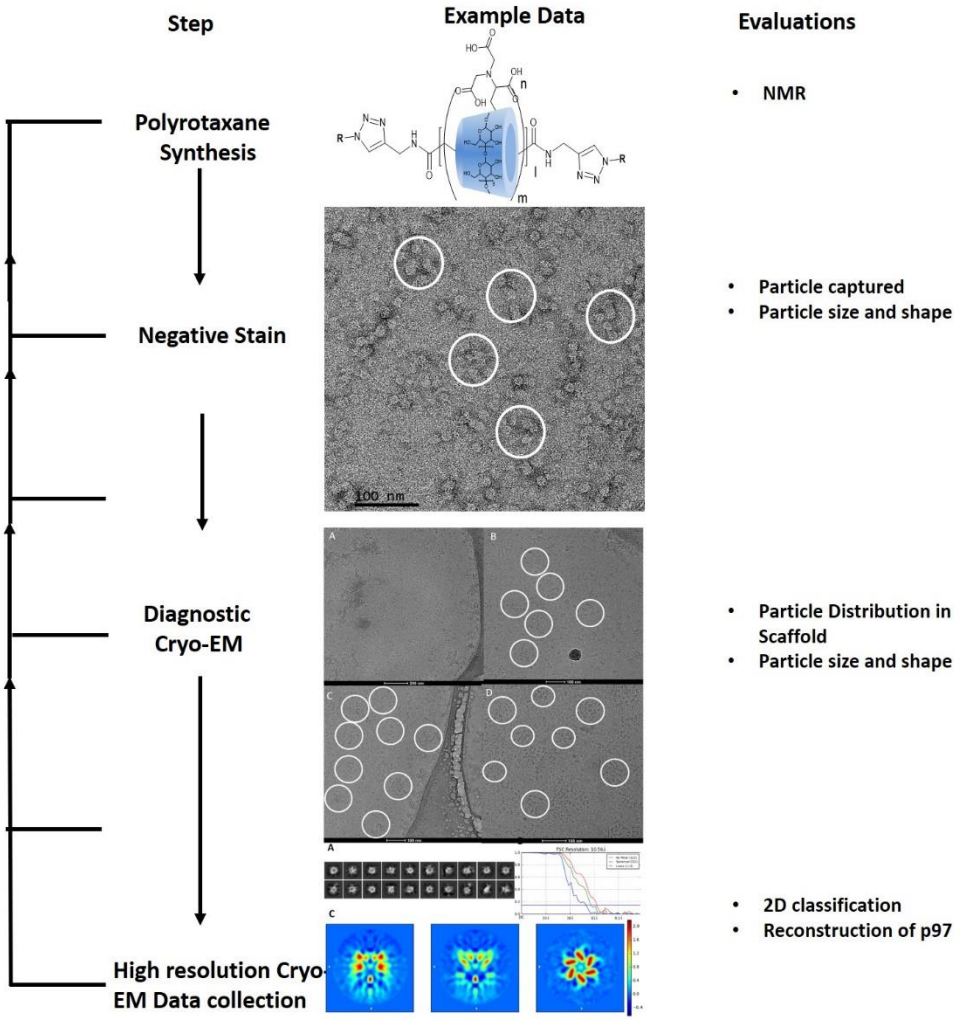

Figure 16: A systematic approach to high resolution p97 structure is shown. In left column, all steps are listed. In middle column, example data are shown for affinity grid approach for p97 (Scale bar are not shown). The right column shows the specific experiment method used for that step.

3.2 Design of Polyrotaxane Based Rod Shaped Scaffold approach

We targeted the generation of new tools for rapid cryoEM sample preparation for single particle 3D reconstruction that can preserve labile protein-protein interactions that are lost in traditional sample preparation methods. These unmet challenges discussed above encourage us to

synthesize polyrotaxane (PR) materials, a class of supramolecular structures where few macrocycles such as cyclodextrins are threaded onto a linear polyethylene glycol (PEG) polymer that has been subsequently end-capped with bulky substituents to prevent dethreading of the macrocycle(s)[20-24]. The macromolecules are also bound to nitrilotriacetic acid (NTA) ligands that will limit non-specific protein adsorption, maximize target protein capture so that they can be employed in cryoEM SPR.

These polyrotaxane materials possess improved beneficial properties due to the non-covalent interactions between polymer (PEG) axle and macrocycle, such as their flexible lateral and rotational mobility of the threaded cyclodextrin that enable their adaptation to the steric demands of the adsorbate. This should result in more unbiased orientations of the concentrated His-tagged protein, a feature that is essential for elucidating its high-resolution structure with cryoEM SPR.

The fundamental aspects of this materials are application of affinity NTA ligands for concentrating of His-tag proteins onto the rod-like scaffold to non-specific protein binding; long, flexible poly(ethylene glycol) (PEG, MW-20,000) tethers between the rod surface plus the NTA affinity ligand to avoid biased sample presentation with respect to the electron beam; and minimization of neighboring protein-protein steric interactions via laterally- and rotationally-adaptable rod-like polyrotaxanes

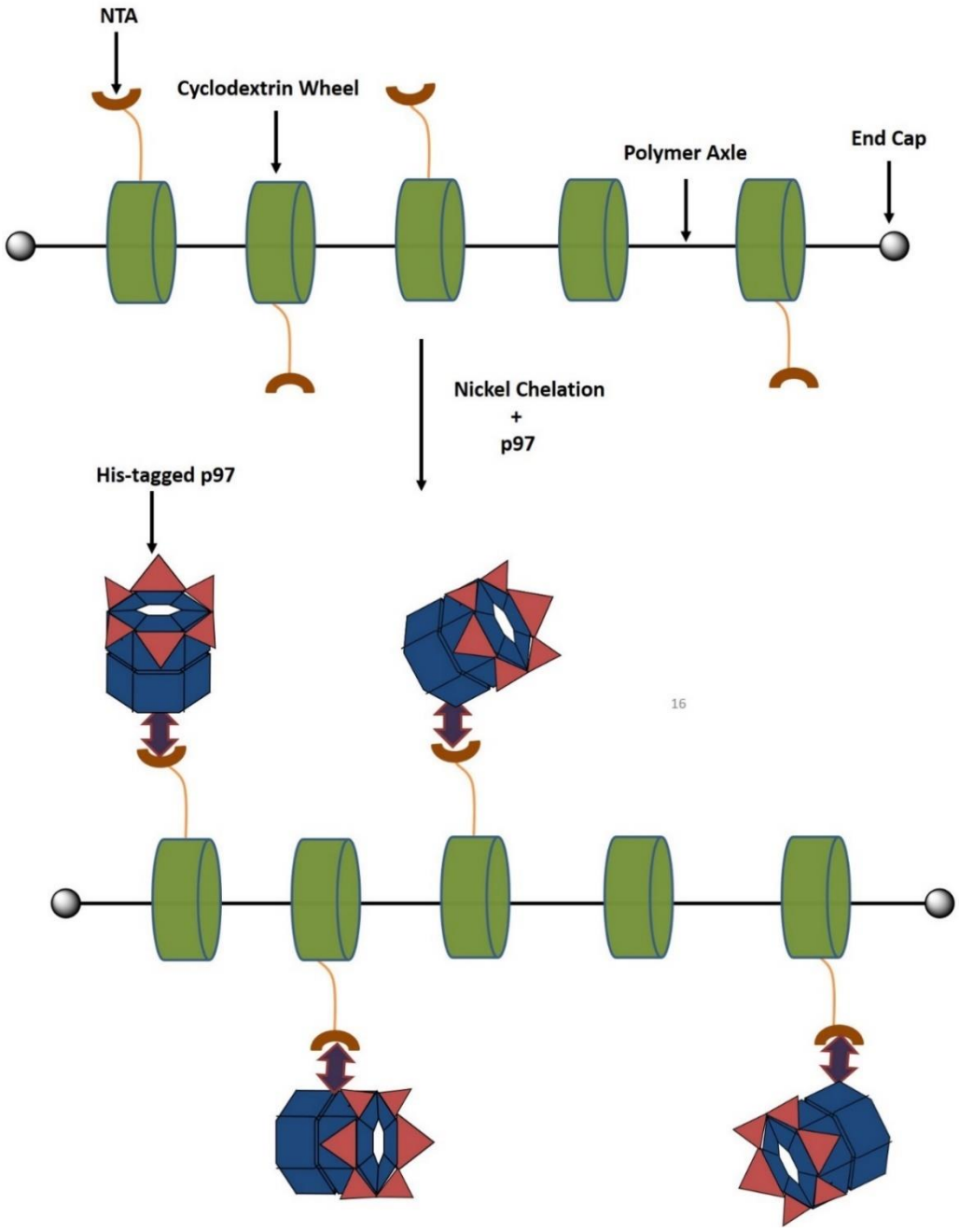

Figure 17: Conceptual diagram of His-Tagged protein bound to the NTA modified polyrotaxane scaffolds.

This strategy employs the NTA:Ni^{2+}:polyhistidine recognition principle on a polyrotaxane based template that contains several laterally- and rotationally-mobile lysine-N_{α},N_{α}-

di(carboxylmethyl)-α-cyclodextrins (LysNTA-α-CD) the to concentrate histidine-tagged proteins on a spatially well-defined scaffold for single particle analysis by cryo-EM. These materials are designed the have good solubility in relevant biological buffers and facilitate SPR of his-tagged proteins since: 1) data collection is accelerated by protein concentration bound to polyrotaxane-NTA surface rather than randomly distributed in solution; (2) polyrotaxanes possesses a constant diameter template at the threaded cyclodextrin core.

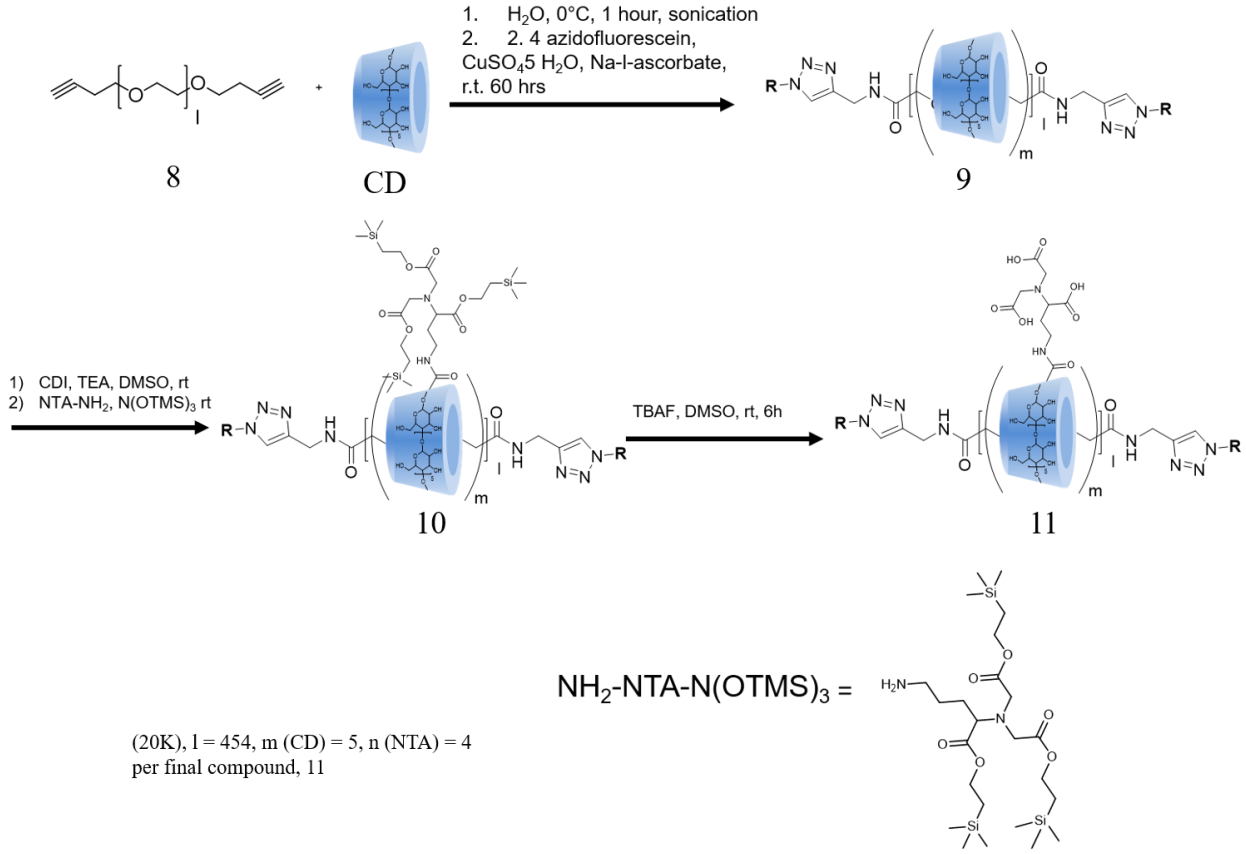

Figure 18: Synthesis scheme for NTA-α-CD:PEG Polyrotaxane.

3.3 Experimental

3.3.1 Synthesis and Characterization of Polyorotaxane Construct

A fluorescein-capped polyrotaxane containing 20,000 PEG units as the axle and α-CD as the macrocycle was synthesized by threading α-CD into PEG chain in aqueous solution followed by rotaxanation via reaction of 5-zzidofluorescein with PEG-bis-alkyne. The polyrotaxanes were isolated by dialysis bag and desalting column. All procedures to develop complete polyrotaxane construct was adapted from work done by Kyle J Wright.

Fluorescein-capped-PEG-α-CD polyrotaxanes (9). α-CD (2.0 g, 2.056. mmol) was dissolved in 200 mL of deionized H_2O, then PEG-bis-alkyne (0.300 gm, 015 mmol) was mixed with the α-CD in solution. The mixture was sonicated for two hours under nitrogen gas at room temperature to form a gel-like substance which was stored in the fume hood for 30 hours. 5-Azidofluorescein in 0.500 mL DMSO (38 mg, 0.102 mmol) was added and the solution was stirred for 30 min. A mixture of 1.0 M $CuSO_4$ solution (25 μL, 0.025 mmol) and 1.0 M sodium-L-ascorbate solution (50 μL, 0.050 mmol) was added via syringe and the solution was stirred for 60 hours at room temperature. The reaction mixture was centrifuged, the supernatant was removed, and the centrifugate was resuspended in 5% EDTA solution and centrifuged. This 5% EDTA treatment was repeated for two times to remove free copper (II) and copper (I). The reaction mixture was washed away with water via 2000 rpm centrifugation, then product was dialyzed with molecular weight 20000 cut off dialyzing bag again DMSO and water for 4 and 5 days respectively. The resulting product was lyophilized to yield a yellow powder of polyrotaxane. Yield: 0.400 gm, ^{1}H NMR (500 MHz, DMSO-d_6) δ 8.00 – 8.12 (m, 1H), 8.20 – 8.40 (m, 1H), 8.45 – 8.60 (m, 1H) 5.50 (d, α-CD-OH), 5.43 (s, α-CD-OH), 4.78 (s, α-CD-OH), 4.50 (t, α-CD-C1-H), 3.90 – 3.08 (m, α-CD and PEG).

TMSE-NTA-Modified-Fluorescein-capped-PEG-α-CD polyrotaxane (10). Fluorescein-capped-Polyrotaxane was dried in a round bottom flask under high vacuum at 50 °C for 4 days. Dry DMSO (10 mL) was added to a 50 mL round bottom flask containing the dried polyrotaxane (0.250 g) and N,N'-carbonyldiimidazole (CDI, 0.300 g). The reaction mixture was allowed to stir for 30 hours at room temperature under Ar gas. The mixture was precipitated using a cold ether-THF solution mixture, then the NTA intermediate (0.100 gm, 0.181 mmol) was added to mixture in 3 mL dry DMSO and triethylamine (0.080 μL) and the reaction stirred for 30 h at room temperature under Ar. The product was purified by dialyzing (molecular weight cut-off 10 kDa) against DMSO and deionized water for 72 hours and 48 hours, respectively. Then the product was lyophilized to give the protected NTA-modified polyrotaxane as a powder. Yield: 0.115 g. ^{1}H NMR (500 MHz, DMSO-d_6) δ 7.90 – 8.10 (m, 1H), 7.80 – 7.88 (m, 1H), 7.00 – 7.20 (m, 1H) 5.50 (d, α-CD-OH), 5.43 (s, α-CD-OH), 4.78 (s, α-CD-OH), 4.50 (t, α-CD-C1-H), 4.47 (s, 3H), 4.21 – 3.99 (m, 6H), 3.90 – 3.08 (m, α-CD and PEG), 3.53 (s, 4H), 3.33 (t, J = 7.5 Hz, 1H), 2.74 (t, J = 7.0 Hz, 2H), 1.63 (dd, J = 14.6, 7.9 Hz, 2H), 1.52 (tt, J = 17.2, 9.3 Hz, 3H), 1.37 – 1.27 (m, 1H), 1.06 – 0.70 (m, 5H), -0.03 (d, J = 4.2 Hz, 25H).

NTA-Modified-Fluorescein-capped-PEG- α-CD polyrotaxane (11). 1.0 M TBAF in THF (0.200 mL) was added to 1 mL DMSO-THF mixture. Compound, 8 (0.100 g) was dissolved in this DMSO-THF mixture. The reaction mixture was stirred at room temperature for 7 hours. The reaction mixture was purified via dialysis (molecular weight cut-off 10 kDa) against DMSO and water for 48 hours and 72 hours, respectively. Fluorescein-capped-NTA-Polyrotaxane was recovered by lyophilization. Then, the product obtained was further purified by Sephadex G-25 gel filtration column chromatography using deionized water as eluent. Pure Polyrotaxane, **8** was collected by lyophilization. ^{1}H NMR (500 MHz, DMSO-d_6) δ 7.90 – 8.10 (m, 1H), 7.80 – 7.88

(m, 1H), 7.00 – 7.20 (m, 1H) 5.50 (d, α-CD-OH), 5.43 (s, α-CD-OH), 4.78 (s, α-CD-OH), 4.50 (t, α-CD-C1-H), 4.47 (s, 3H), 4.21 – 3.99 (m, 6H), 3.90 – 3.08 (m, α-CD and PEG), 3.53 (s, 4H), 3.33 (t, J = 7.5 Hz, 1H), 2.74 (t, J = 7.0 Hz, 2H), 1.63 (dd, J = 14.6, 7.9 Hz, 2H), 1.52 (tt, J = 17.2, 9.3 Hz, 3H), 1.37 – 1.27 (m, 1H), 1.06 – 0.70 (m, 5H).

H_2N-Lys-NTA-(OTMSE). A mixture of lysine NTA intermediate (10.62 g, 26.8 mmol), 2-(trimethylsilyl)ethanol (19.01 g, 160.8 mmol) and DMAP (2.45 g, 20.1 mmol) were added to an dried 250 mL round bottom flask equipped with a magnetic stir bar and a rubber septum. The mixture was dissolved in a 4:1 DMF:pyridine solution (250 mL) and cooled down to 0 °C in an ice bath and EDC (16.22 g, 84.6 mmol) was added. The solution was stirred for 30 hours and gradually warming to room temperature. The solution was concentrated and dissolved in Et_2O (200 mL), filtered, and the filtrate was extracted with 5 % HCl (80 mL) twice. The organic phase was dried over anhydrous $MgSO_4$, concentrated, and purified by column chromatography using 4:1 hexane:EtOAc as eluent. The pure fractions were combined, concentrated and dried in vacuo to give the NTA-(OTMSe) intermediate as a clear oil. Then, NTA-(OTMSe) intermediate (0.743 g, 1.31 mmol) was suspended in DCM (35 mL). DIEA (0.171 g, 1.32 mmol) was added via syringe followed by succinic anhydride (0.198 g, 1.98 mmol) and the solution stirred for 30 hours under N_2 at ambient temperature. The solution was concentrated and redissolved in Et_2O (150 mL). The solution was extracted with 0.1 M HCl (50 mL) twice, then the ether phase was dried with anhydrous $MgSO_4$, concentrated, and purified using a gradient of 8 % MeOH/DCM to 20 % MeOH/DCM. The pure fractions were combined, concentrated and dried *in vacuo* to give Compound NH_2-Lys-NTA-(OTMSe) as a clear oil. Yield: 0.805 g (92.0 %). ^{1}H NMR (500 MHz, $CDCl_3$) δ 9.22 (s, 1H), 6.70 (s, 1H), 4.13 (dd, J = 11.1, 5.6 Hz, 6H), 3.73 – 3.62 (m, 1H), 3.56 (d, J = 12.5 Hz, 3H), 3.38 (t, J = 7.5 Hz, 1H), 3.21 (dd, J = 12.0, 5.5 Hz, 2H), 2.61 (dd, J = 13.9, 7.0

Hz, 3H), 2.52 (d, J = 6.3 Hz, 2H), 1.79 – 1.60 (m, 2H), 1.58 – 1.34 (m, 4H), 1.32 – 1.10 (m, 1H), 0.95 (q, J = 8.1 Hz, 6H), -0.00 (d, J = 4.7 Hz, 25H).

Ni^{2+} activation of NTA-polyrotaxane. Polyrotaxane **(12)** (20 mg) was dissolved in o.2 mL of 20 mM Ni^{2+} solution and the excess Ni^{2+} removed by mini gel filtration Bio-Rad column (Cut-off MW 10,000 da). After lyophilization, the Ni^{2+} activated PR was obtained as a solid (12 mg).

3.3.2 Preparation of Polyrotaxane-modified grid for TEM

1 mg/mL of polyrotaxane-NTA-Ni^{2+} and different concentrations of p97 mixture were applied to glow discharged lacey/UC lacey girds followed by washing the grids 2-3 times with 15 µL Tris buffer. A 3-5 µL drop of 1 % uranyl acetate was applied on the grid and incubated for at least 1 minute, then excess solution was removed using a wedge of filter paper and completely dried under vacuum for 1 hour. Negatively stained images were recorded using a Tecnai T-20 transmission electron microscope operating at 200 kV.

3.3.3 Preparation of Frozen Hydrated Samples for Cryo-EM.

For cryo-EM imaging, 4 µL of a mixed solution of 200 nM **11**-Ni^{2+}- p97 (3.0 µM 2:1 his_6-tagged-p97: α-CD stoichiometry) in 10 mM Tris buffer (pH 7.4) were spread onto glow discharged UC/Lacey grids then plunge-frozen in liquid ethane with 7 second blotting time using cryo-Plunger-3 (CP3).

3.3.4 Image Processing

A cryo-EM dataset using 25,000 particles that generated a map with a resolution of 10.56 Å. A total of 10,000 isometric particles were boxed from 30 images. 2D classification was performed with the Relion program to select 25,000 particles. The jspr program was used to generate initial model and refinement of the particle orientations, assuming C6 symmetry. The final 3D cryo-EM

reconstruction has an overall 10.56 Å resolution, based on the "gold-standard" Fourier shell correlation (FSC) using the FSC = 0.143 criterion. We have chosen 2 class averages from total 50 class averages to produce an initial model that imposed with C6 symmetry (Figure 7 C). We have produced a gold standard (0.143 criteria) density map with 10.56 Å resolution requires several refinement iterations using conservative masking. An uneven distribution of defocuses in micrograph visible nodes in the FSC curve at regular intervals (Figure 7 B).

3.4 Result and Discussion.

Polyrotxanes were analysed by NMR to evaluate comparative threading efficiency and molecular weight. The threading efficiency of unmodified polyrotaxane, **9** is 26 (11%) is based on hypothesis that each CD unit can occupy maximum of two PEG units from 227 units long PEG polymer chain, then threaded CD number decreased to around five copies in NTA modified polyrotaxane, **11**. ^{1}H-NMR analysis of Compound, **10** reveals that there are four NTA group per cyclodextrin. NMR data for Compound **10** and **11** collectively shows that there are around 20 NTA groups per polyrotaxane. ^{1}H-NMR analysis was also used to evaluate the threading efficiency of cyclodextrin onto PEG axle. We infer from these findings that threaded CD number was 65, which decreased to 25 in the second step and 5 in final step to give an estimated molecular weight of 36 kDa.

Entry	PEG MW	Threading %	CD's Threaded	MW (NMR)
9	20000 (227 PEG Unit)	27	65	83.1 kDa
10		11	26	102.3 kDa
11		2	5	35 kDa

Figure 19: Characterization of NTA-Modified Fluorescein-Capped Polyrotaxanes

To quantify the Ni^{2+} chelation capacity of **12**, the total Ni^{2+} content bound to NTA was analyzed by ICP-MS. A solution of 20 mM $NiSO_4$ was added to **11,** followed by isolation and purification via Bio-Rad desalting column (MW cut off 10000). ICP-MS analysis of the purified material revealed a Ni^{2+} content corresponding to approximately 6 NTA units per polyrotaxane.

In order to evaluate potential application of polyrotaxane-NTA-Ni^{2+} complex for single particle analysis, first we performed negative stained imaging was performed using p97 in Tecnai-T-20. Negative stained imaging of **11**-Ni^{2+}-p97 complex showed appearance of rod and coiled shaped structures. Micrographs obtained from the TEM analysis disclosed that there are three to eight particles that are distributed along a linear configuration (Figure 4C), while some assemblies were also organized in coiled shape (Figure 4A, 4B). We have analyzed **11**-Ni^{2+}-p97 complex by keeping the polyrotaxane concentration constant and varying the p97 concentration as our hypothesis is that concentrated target particles onto polyrotaxane scaffold can be easily visualized with fixed concentration of polyrotaxane. When 1 mg/mL of **11**-Ni^{2+} and 0.400 mg/mL of p97 mixture was applied on a glow discharged lacey grid, a lot of rod-shaped particles orientation are observed clearly (Figure 4D). In some cases, around 12-15 particles in a line were observed. Our hypothesis is that a high concentration of particles may increase particle-particle interaction, leading to two or more rods to become associated combine. When the protein concentration decreases from 400 to 300 µg/mL, more-clear linear and circular orientation of particle's were observed (Figure 4A, 4B and 4C). Raw images from 0.400 mg/mL (Figure 4E) and 500 µg/mL (Figure 4F) of p97 onto glow-discharged lacey grid are shown as controls.

Next, a cryo-EM study of **11**-Ni^{2+}-p97 complexes was performed. **11**-Ni^{2+}-p97 modified grids were prepared using a 7 second blotting time prior to cryofixation via cryo-Plunger-3 (CP3). It was hard to identify concentrated p97 onto the polyrotaxane scaffold as highly concentrated p97

mixed with **11**-Ni^{2+} was applied on glow discharged lacey carbon grid (Figure-5A). Our hypothesis is that excessive amount of p97 was non-specifically adsorbed on grid surface, making it difficult to distinguish between free and bound p97. When the protein concentration was decreased, particles around the polyrotaxane scaffolds were more clearly visualized.

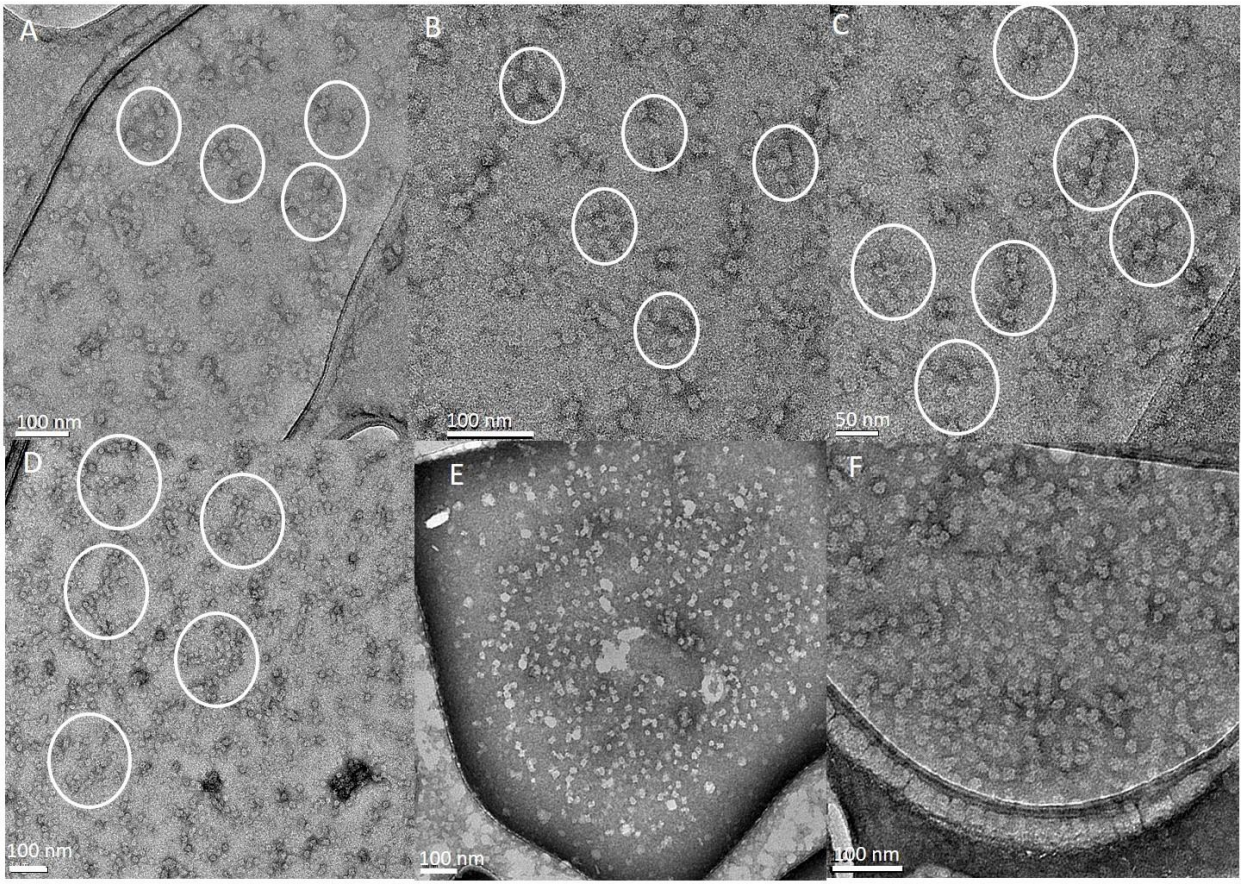

Figure 20: Glow discharged lacey carbon grid coated with different ratio of Polyrotaxane-NTA-Ni^{2+}: p97. Raw TEM image displaying p97 hexamer particles; several representative molecular images are circled, captured from mixture of (A) 3 µL of 1 mg/mL polyrotaxane-Ni^{2+} and 3 µL of 300 µg/mL of p97, (B) 3 µL of 1 mg/mL polyrotaxane-Ni^{2+} and 3 µL of 350 µg/mL of p97, (C) 3 µL of 1 mg/mL polyrotaxane-Ni^{2+} and 3 µL of 400 mg/mL of p97, (D) 3 µL of 1 mg/mL polyrotaxane-Ni^{2+} and 3 µL of 1 mg/mL of p97, (E) 3 µL of 500 µg/mL of p97 applied on glow discharged lacey grid, (F) 3 µL of 1 mg/mL of p97 applied on glow discharged lacey grid.

Figure 5B and 5C shows 6-8 particle's concentrated on scaffolds where 5D shows 12 to 20 particles onto scaffolds, which reflects the likelihood that higher concentration may have increased

protein-protein interactions leading to p97 scaffold aggregation. When the particle concentration was lowered (300 and 200 μg/mL), the particle density showed many more linear configuration (Figure 6A, D and 6B, E). Figure 6C, F shows that the polyrotaxane scaffold didn't collect enough p97 to concentrate well onto the grid surface.

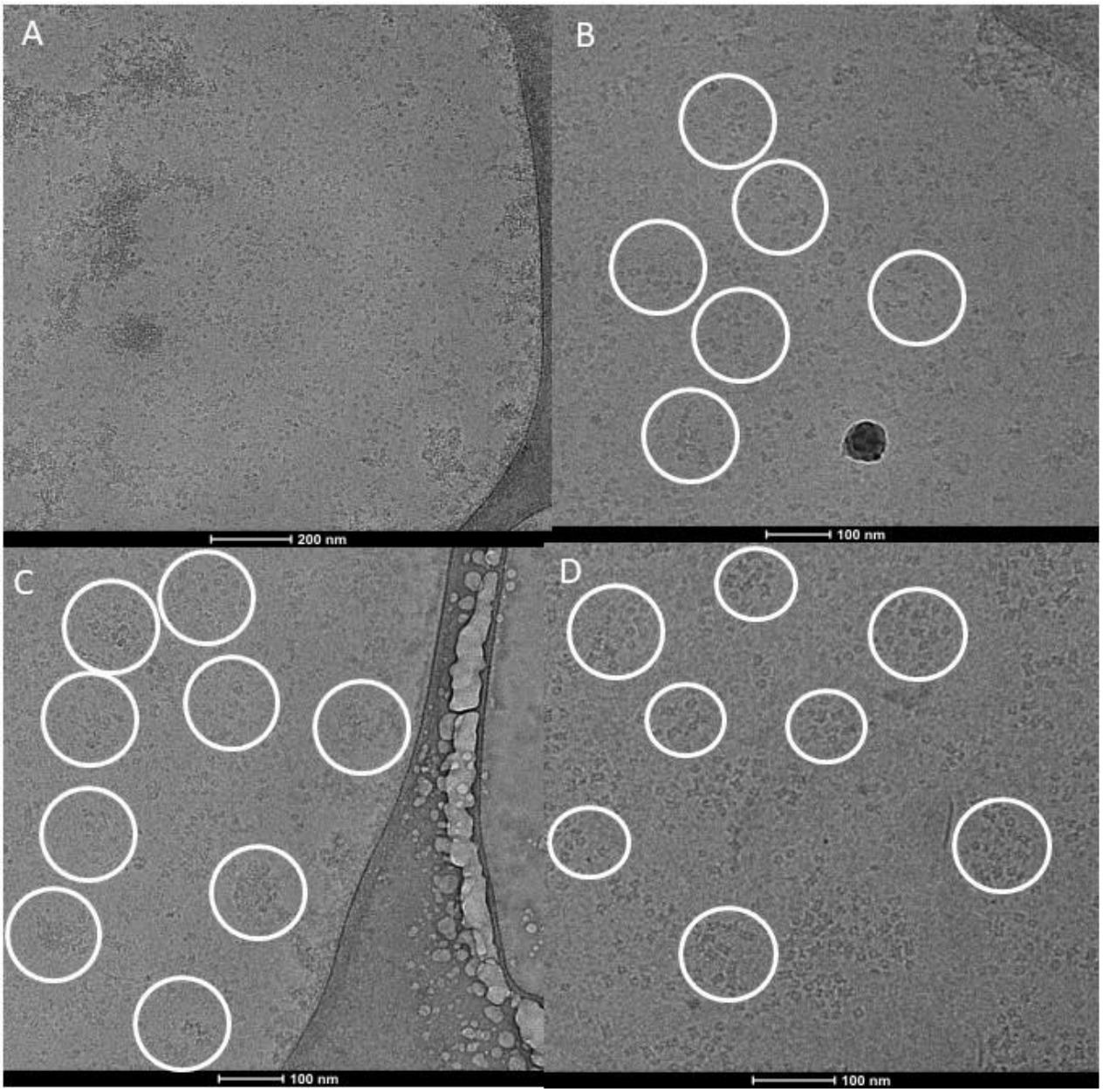

Figure 21: Glow discharged lacey carbon grid coated with different ratio of Polyrotaxane-NTA-Ni^{2+}:p97. Raw image displaying p97 hexamer particles; several representative molecular images are circled, captured from mixture of (A) 3 µL of 1 mg/mL polyrotaxane-Ni^{2+} and 3 µL of 1 mg/mL of p97, (B) 3 µL of 1 mg/mL polyrotaxane-Ni^{2+} and 3 µL of 400 µg/mL of p97, (C) 3 µL of 1 mg/mL polyrotaxane-Ni^{2+} and 3 µL of 500 µg/mL of p97, (D) 3 µL of 1 mg/mL polyrotaxane-Ni^{2+} and 3 µL of 600 µg/mL of p97 on glow discharged lacey grid.

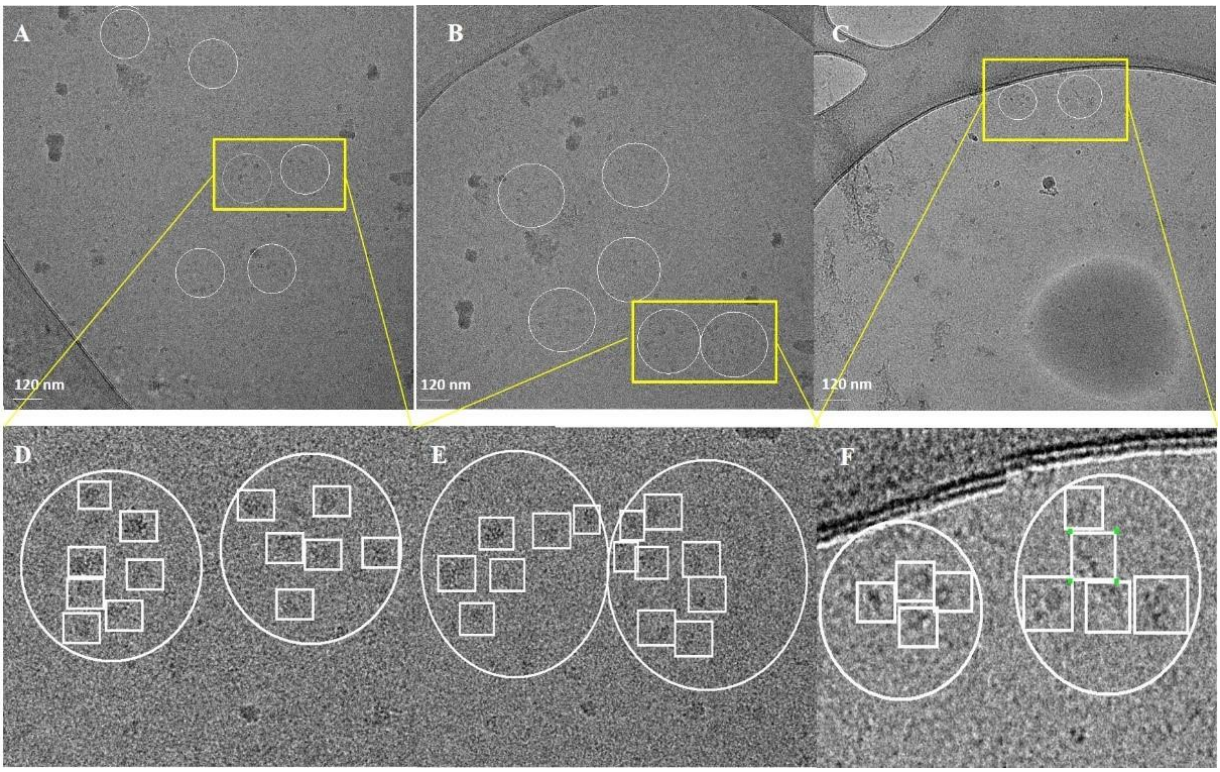

Figure 22: Glow discharged lacey carbon grid coated with different ratio of **9**-Ni^{2+}:p97. Raw image displaying p97 hexamer particles; several representative molecular images are circled, captured from mixture of (A,D) 3 µL of 1 mg/mL polyrotaxane-Ni^{2+} and 3 µL of 300 µg/mL of p97, (B,E) 3 µL of 1 mg/mL polyrotaxane-Ni^{2+} and 3 µL of 200 µg/ml of p97, (C,F) 3 µL of 1 mg/mL polyrotaxane-Ni^{2+} and 3 µL of 100 µg/mL of p97 on glow discharged lacey grid.

Taking negative stained and cryo-EM imaging data in consideration, we infer from our results that there are linear, spherical and coiled shaped arrangements of polyrotaxane:p97 complex.

In order to further evaluate the ability of polyrotaxane compound to employ lateral and rotational motion of adsorbed particles to avoid preferred p97 orientations, we have performed 2D classification of datasets collected using the TALOS FEI camera and processed via cryo-SPARC.

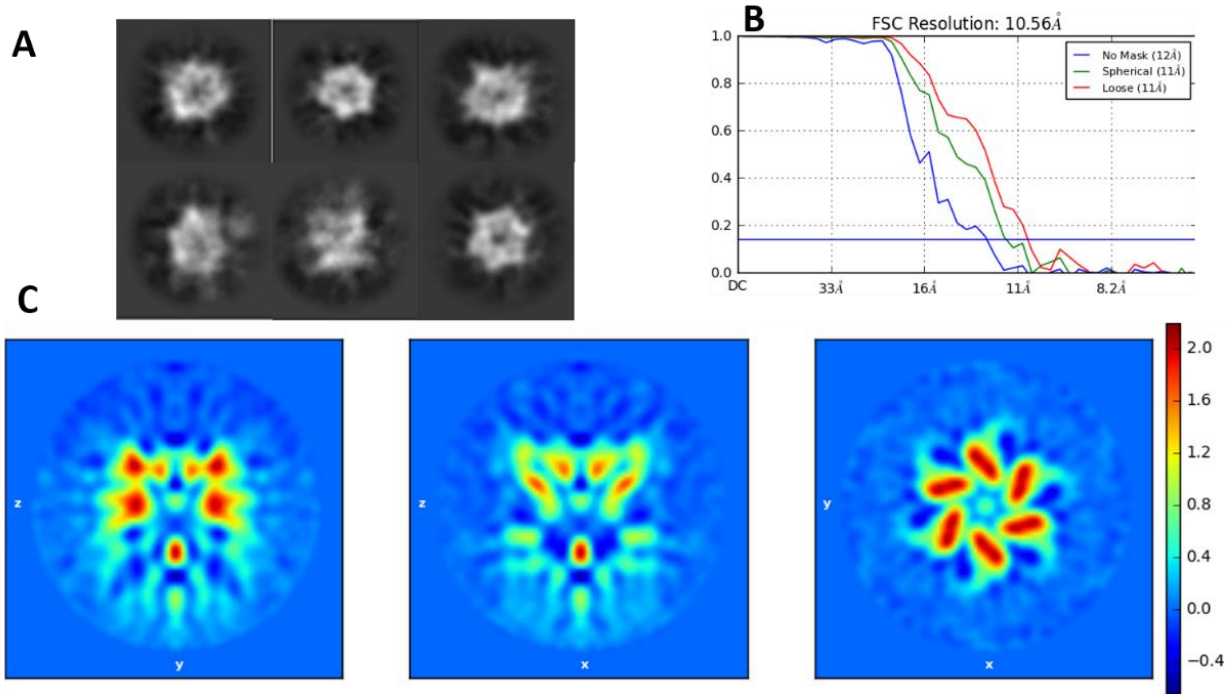

Figure 23: Intermediate stages in structure determination of wild-type p97. (A) 2D class averages showing that both top and side views are represented in the data, (B) gold standard (0.143 criteria) density map with 10.56 Å resolution using conservative masking, (C) Sections through cryo-EM density map of native p97 from ab initio model.

2-D reference-free classification in *cryoSPARC* shows top view and side view of p97 (Figure 7A) which generated *ab initio* model with a resolution of 10.56 Å of p97 (Figure 7C).

3.5 Conclusions

A polyrotaxane molecule based on a 20,000 PEG core, alpha cyclodextrin beads and fluorescein as end cap was synthesized. Our polyrotaxane scaffold is expected to work for concentrating any his-tagged particle on TEM grid. According to our expectation, we have seen from NMR that every scaffold may have maximum 20 NTA which can capture as many as 20 his-tagged particles which is consistent without negative staining and cryo-EM imaging observations. Our anticipation was that rotational and lateral flexibility of alpha cyclodextrin units threaded onto the PEG axle may

help to avoid preferred orientation of particle which agrees with cryo-EM imaging and reconstruction of p97. Our findings are consistent with this expectation.

3.6 Acknowledgements

A p97 plasmid for single particle cryo-EM analysis was a gift provided by Tsui-Fen Chou at University of California, Los Angeles.

3.7 References

1. Bartesaghi, A.; Merk, A.; Banerjee, S.; Matthies, D.; Wu, X.; Milne, J. L.; Subramaniam, S., 2.2 Å resolution cryo-EM structure of β-galactosidase in complex with a cell-permeant inhibitor. *Science* **2015,** *348*, 1147-1151.

2. Banerjee, S.; Bartesaghi, A.; Merk, A.; Rao, P.; Bulfer, S. L.; Yan, Y.; Green, N.; Mroczkowski, B.; Neitz, R. J.; Wipf, P.; Falconieri, V.; Deshaies, R. J.; Milne, J. L.; Huryn, D.; Arkin, M.; Subramaniam, S., 2.3 Å resolution cryo-EM structure of human p97 and mechanism of allosteric inhibition. *Science* **2016,** *351*, 871-875.

3. Gong, X.; Qian, H.; Zhou, X.; Wu, J.; Wan, T.; Cao, P.; Huang, W.; Zhao, X.; Wang, X.; Wang, P.; Shi, Y.; Gao, G. F.; Zhou, Q.; Yan, N., Structural insights into the Niemann-Pick C1 (NPC1)-mediated cholesterol transfer and Ebola infection. *Cell* **2016,** *165*, 1467-1478.

4. Blok, N. B.; Tan, D.; Wang, R. Y.; Penczek, P. A.; Baker, D.; DiMaio, F.; Rapoport, T. A.; Walz, T., Unique double-ring structure of the peroxisomal Pex1/Pex6 ATPase complex revealed by cryo-electron microscopy. *Proceedings of the National Academy of Sciences of the United States of America* **2015,** *112*, E4017-E4025.

5. Cheng, Y., Single-particle cryo-EM at crystallographic resolution. *Cell* **2015,** *161*, 450-457.

6. Henderson, R., Overview and future of single particle electron cryomicroscopy. *Archives of Biochemistry & Biophysics* **2015,** *581*, 19-24.

7. Henderson, R.; McMullan, G., Problems in obtaining perfect images by single-particle electron cryomicroscopy of biological structures in amorphous ice. *Microscopy* **2013,** *62*, 43-50.

8. Milazzo, A. C.; Cheng, A.; Moeller, A.; Lyumkis, D.; Jacovetty, E.; Polukas, J.; Ellisman, M. H.; Xuong, N. H.; Carragher, B.; Potter, C. S., Initial evaluation of a direct detection device detector for single particle cryoelectron microscopy. *Journal of Structural Biology* **2011,** *176*, 404-408.

9. Suloway, C.; Pulokas, J.; Fellmann, D.; Cheng, A.; Guerra, F.; Quispe, J.; Stagg, S.; Potter, C. S.; Carragher, B., Automated molecular microscopy: the new Leginon system. *Journal of Structural Biology* **2005,** *151*, 41-60.

10. Suloway, C.; Shi, J.; Cheng, A.; Pulokas, J.; Carragher, B.; Potter, C. S.; Zheng, S. Q.; Agard, D. A.; Jensen, G. J., Fully automated, sequential tilt-series acquisition with Leginon. *Journal of Structural Biology* **2009,** *167*, 11-18.

11. Taylor, D. W.; Kelly, D. F.; Cheng, A.; Taylor, K. A., On the freezing and identification of lipid monolayer 2-D arrays for cryoelectron microscopy. *Journal of Structural Biology* **2007,** *160*, 305-312.

12. Kelly, D. F.; Abeyrathne, P. D.; Dukovski, D.; Walz, T., The affinity grid: a pre-fabricated EM grid for monolayer purification. *Journal of Molecular Biology* **2008,** *382*, 423-433.

13. Yu, G.; Vago, F.; Zhang, D.; Snyder, J. E.; Yan, R.; Zhang, C.; Benjamin, C. J.; Jiang, X.; Kuhn, R. J.; Serwer, P.; Thompson, D. H.; Jiang, W., Single-step antibody-based affinity cryo-electron microscopy for imaging and structural analysis of macromolecular assemblies. *Journal of Structural Biology* **2014,** *187*, 1-9.

14. Kiss, G.; Chen, X.; Brindley, M. A.; Campbell, P.; Afonso, C. L.; Ke, Z.; Holl, J. M.; Guerrero-Ferreira, R. C.; Byrd-Leotis, L. A.; Steel, J.; Steinhauer, D. A.; Plemper, R. K.; Kelly, D. F.; Spearman, P. W.; Wright, E. R., Capturing enveloped viruses on affinity grids for downstream cryo-electron microscopy applications. *Microscopy & Microanalysis* **2014,** *20*, 164-174.

15. Benjamin, C. J.; Wright, K. J.; Bolton, S. C.; Hyun, S.-H.; Krynski, K.; Grover, M.; Yu, G.; Guo, F.; Kinzer-Ursem, T. L.; Jiang, W.; Thompson, D. H., Selective capture of histidine-tagged proteins from cell lysates using TEM grids modified with NTA-graphene oxide. *Sci. Rep.* **2016,** *6*, 32500.

16. Benjamin, C. J.; Wright, K. J.; Hyun, S.-H.; Krynski, K.; Yu, G.; Bajaj, R.; Guo, F.; Stauffacher, C. V.; Jiang, W.; Thompson, D. H., Nonfouling NTA-PEG-based TEM grid coatings for selective capture of histidine-tagged protein targets from cell lysates. *Langmuir* **2016,** *32* (2), 551-559.

17. Dong, Y.; Liu, Y.; Jiang, W.; Smith, T. J.; Xu, Z.; Rossmann, M. G., Antibody-induced uncoating of human rhinovirus B14. *Proceedings of the National Academy of Sciences* **2017,** *114* (30), 8017-8022.

18. Russo, C. J.; Passmore, L. A., Controlling protein adsorption on graphene for cryo-EM using low energy hydrogen plasmas. *Nature Methods* **2014,** *11*, 649-652.

19. Gonen, S.; DiMaio, F.; Gonen, T.; Baker, D., Design of ordered two-dimensional arrays mediated by noncovalent protein-protein interfaces. *Science* **2015,** *348*, 1365-1368.

20. Harada, A.; Kamachi, M., Complex-Formation between Poly(Ethylene Glycol) and Alpha-Cyclodextrin. *Macromolecules* **1990,** *23* (10), 2821-2823.

21. Stoddart, J. F.; Belowich, M. E.; Valente, C., Template-Directed Syntheses of Rigid Oligorotaxanes under Thermodynamic Control. *Angew Chem Int Edit* **2010,** *49*, 7208-7212.

22. Ooya, T.; Yui, N., Polyrotaxanes: Synthesis, Structure, and Potential in Drug Delivery. *Crit Rev Ther Drug* **1999,** *16*, 289-330.

23. Miyake, K.; Yasuda, S.; Harada, A.; Sumaoka, J.; Komiyama, M.; Shigekawa, H., Formation Process of Cyclodextrin Necklace - Analysis of Hydrogen Bonding on a Molecular Level. *J Am Chem Soc* **2003,** *125*, 5080-5085.

24. Yui, N.; Ooya, T., Synthesis of theophylline-polyrotaxane conjugates and their drug release via supramolecular dissociation. *J Control Release* **1999,** *58* (3), 251-269.

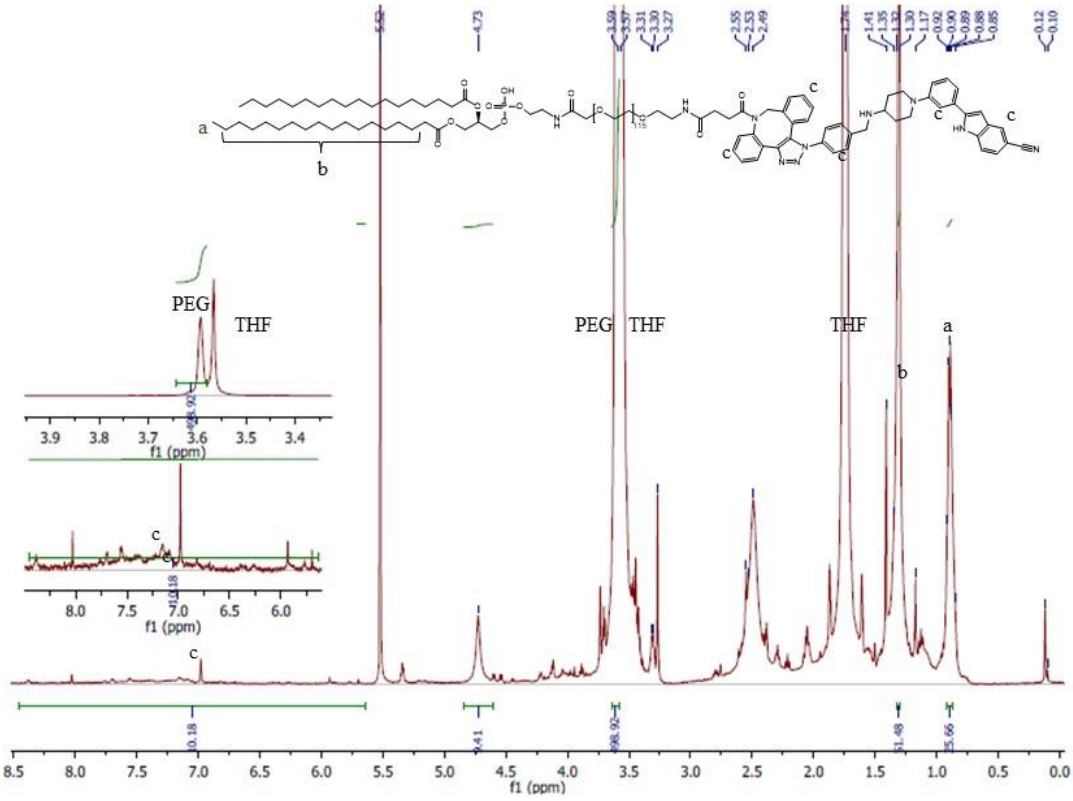

Figure 24: ^{1}H-NMR of Conjugate-1

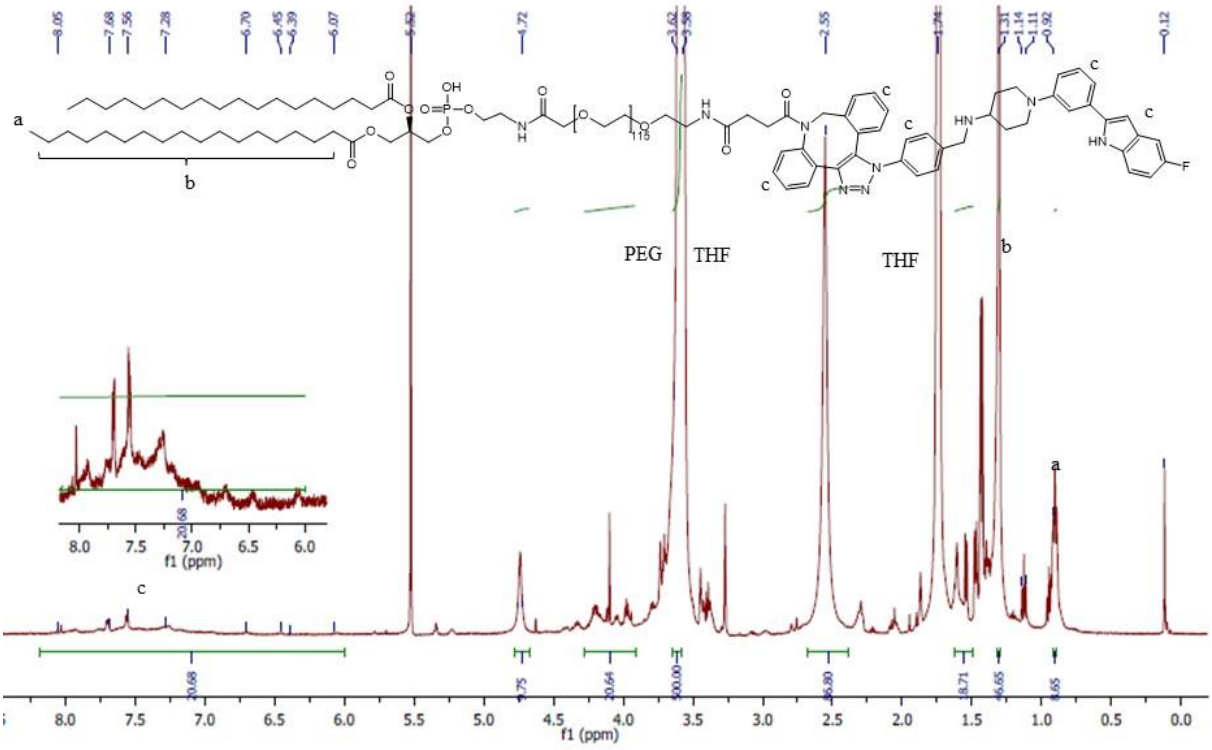

Figure 25: ^{1}H-NMR of Conjugate-2

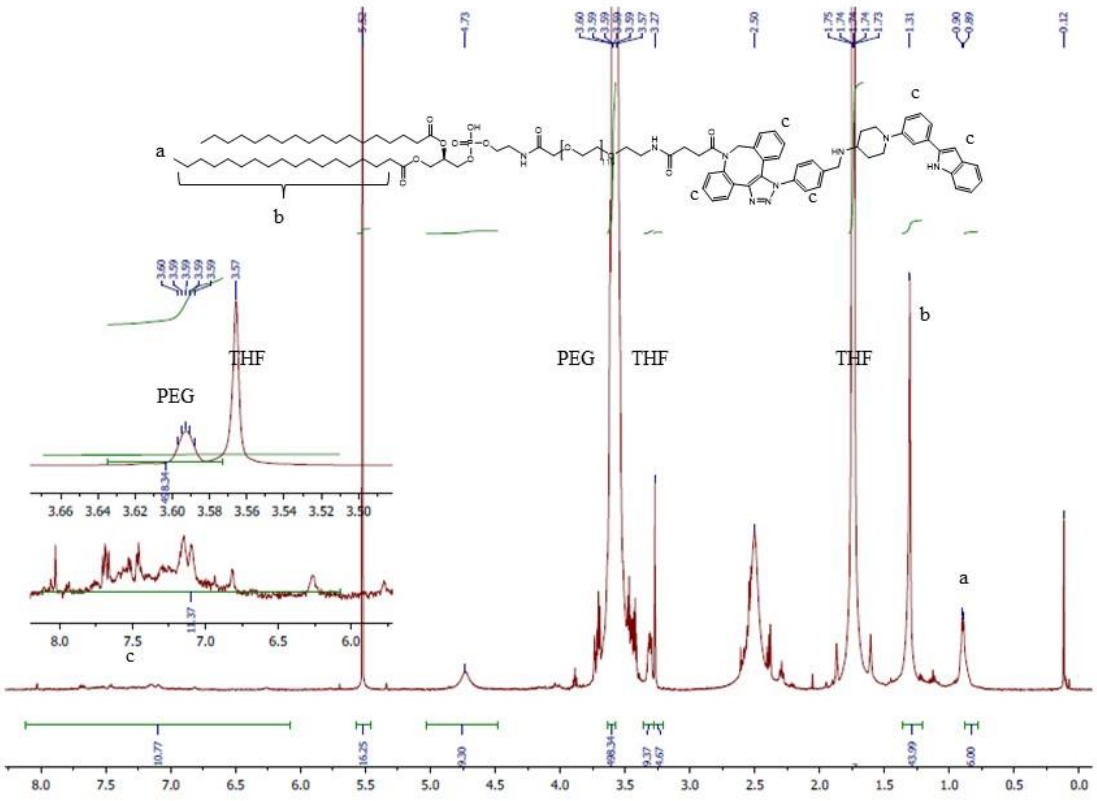

Figure 26: ^{1}H-NMR of Conjugate-3

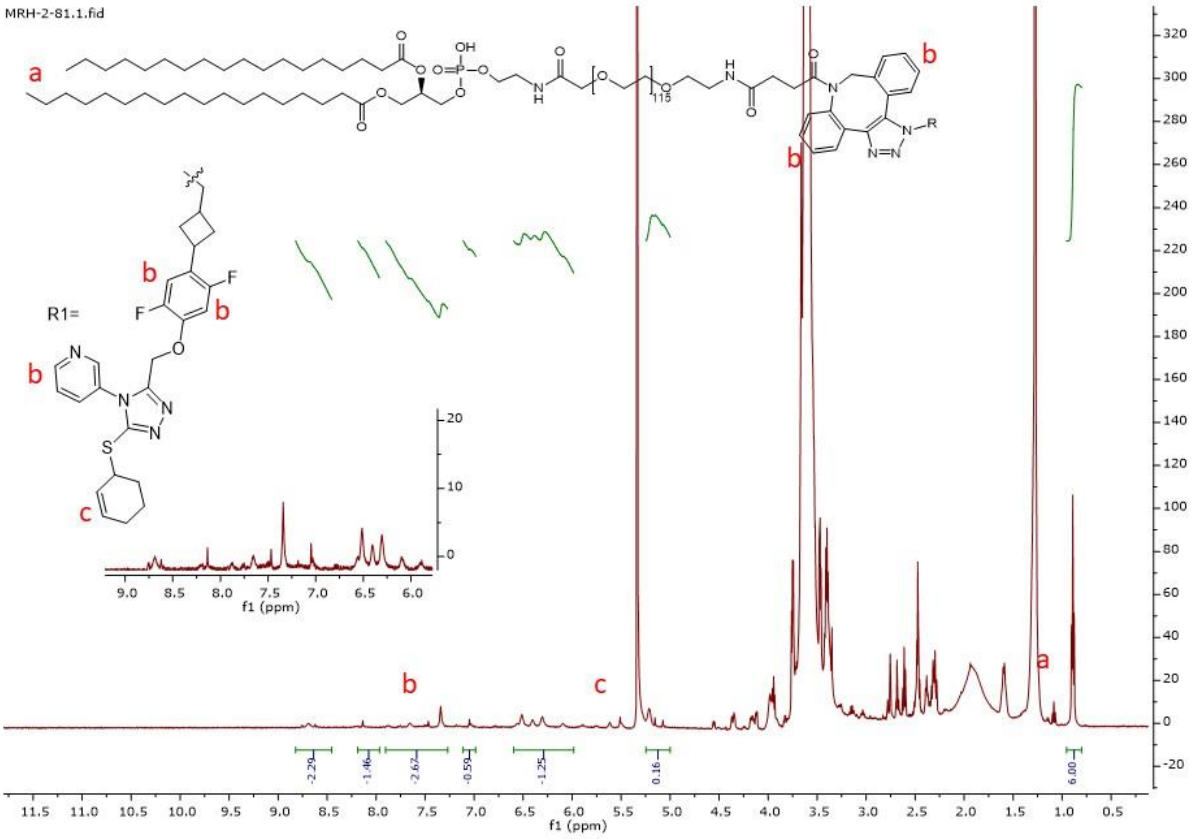

Figure 27: ^{1}H-NMR of Conjugate-4

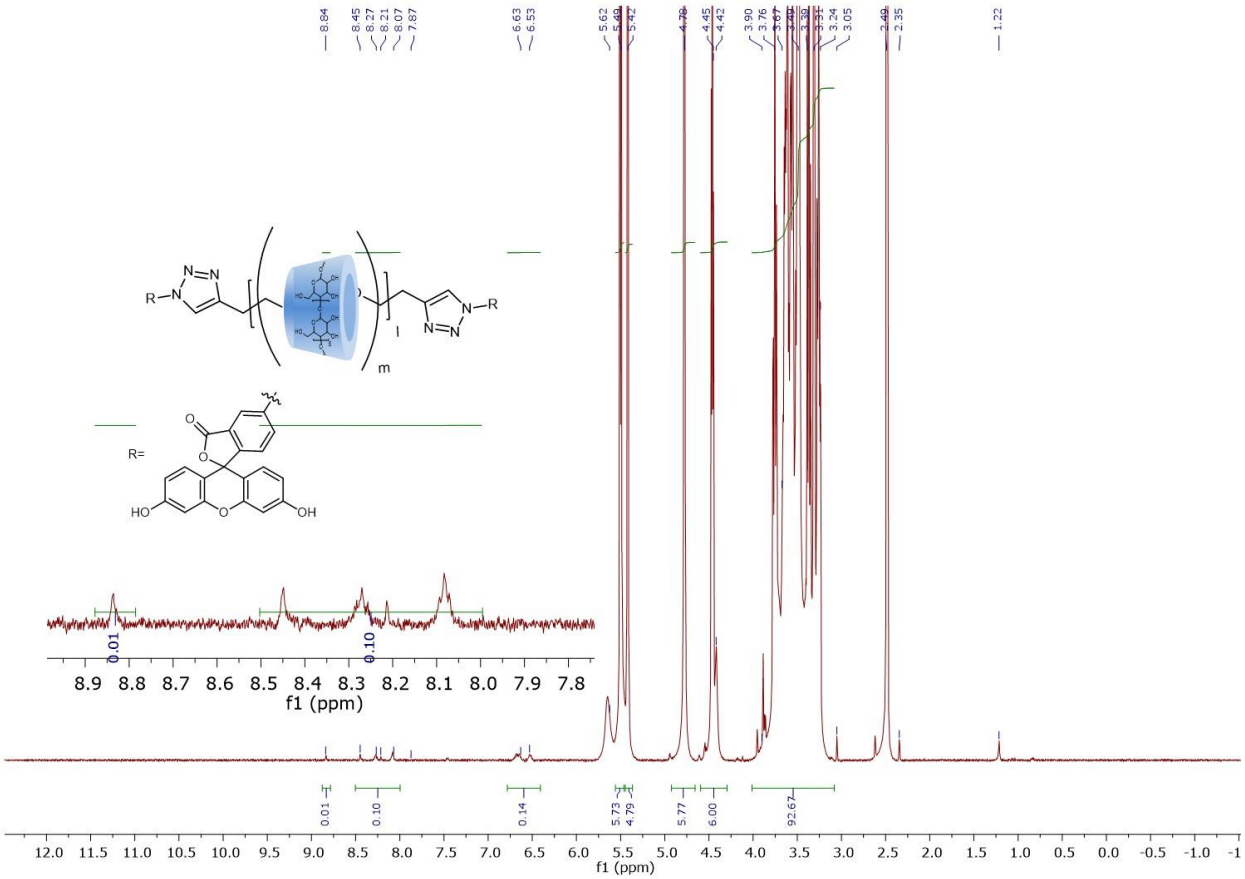

Figure 28: ^{1}H-NMR of Compound-9

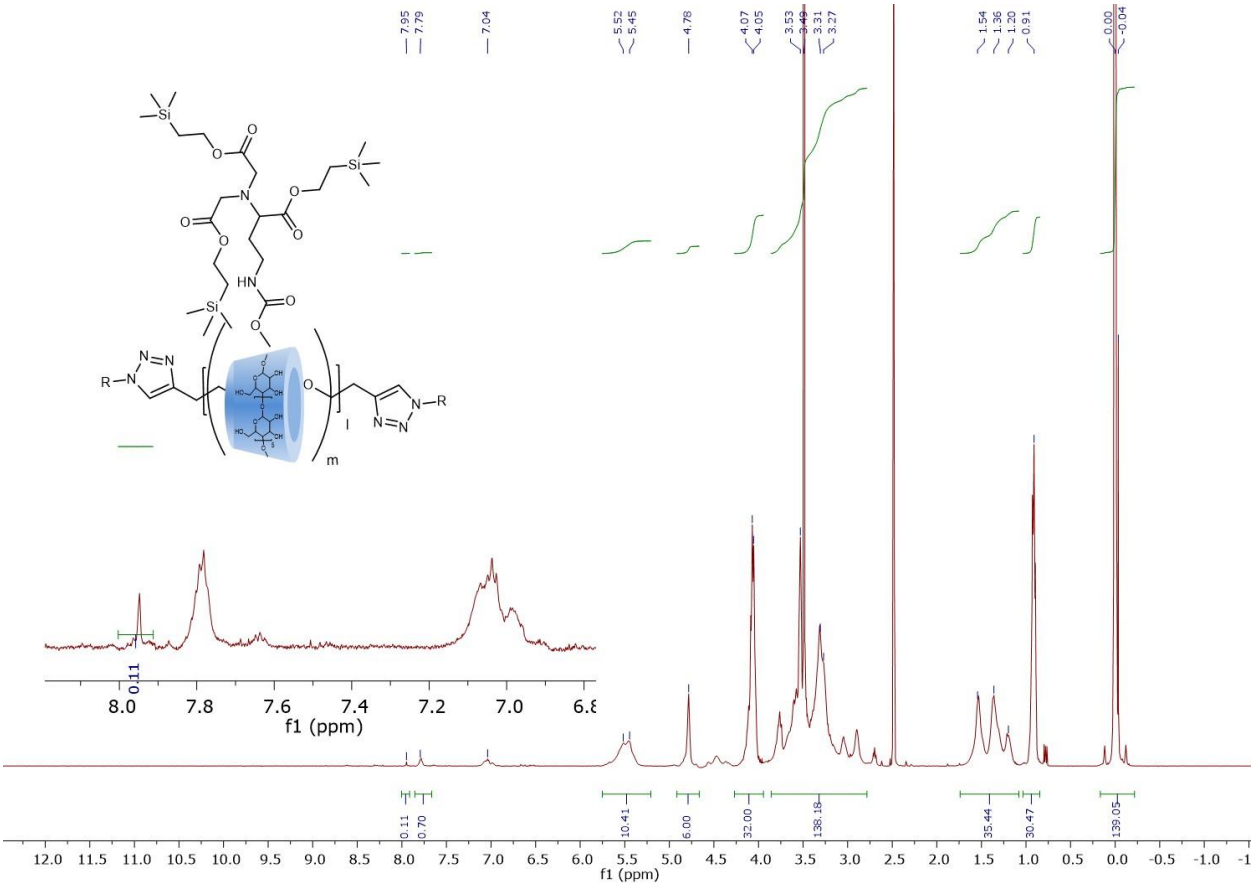

Figure 29: ^{1}H-NMR of Compound-10

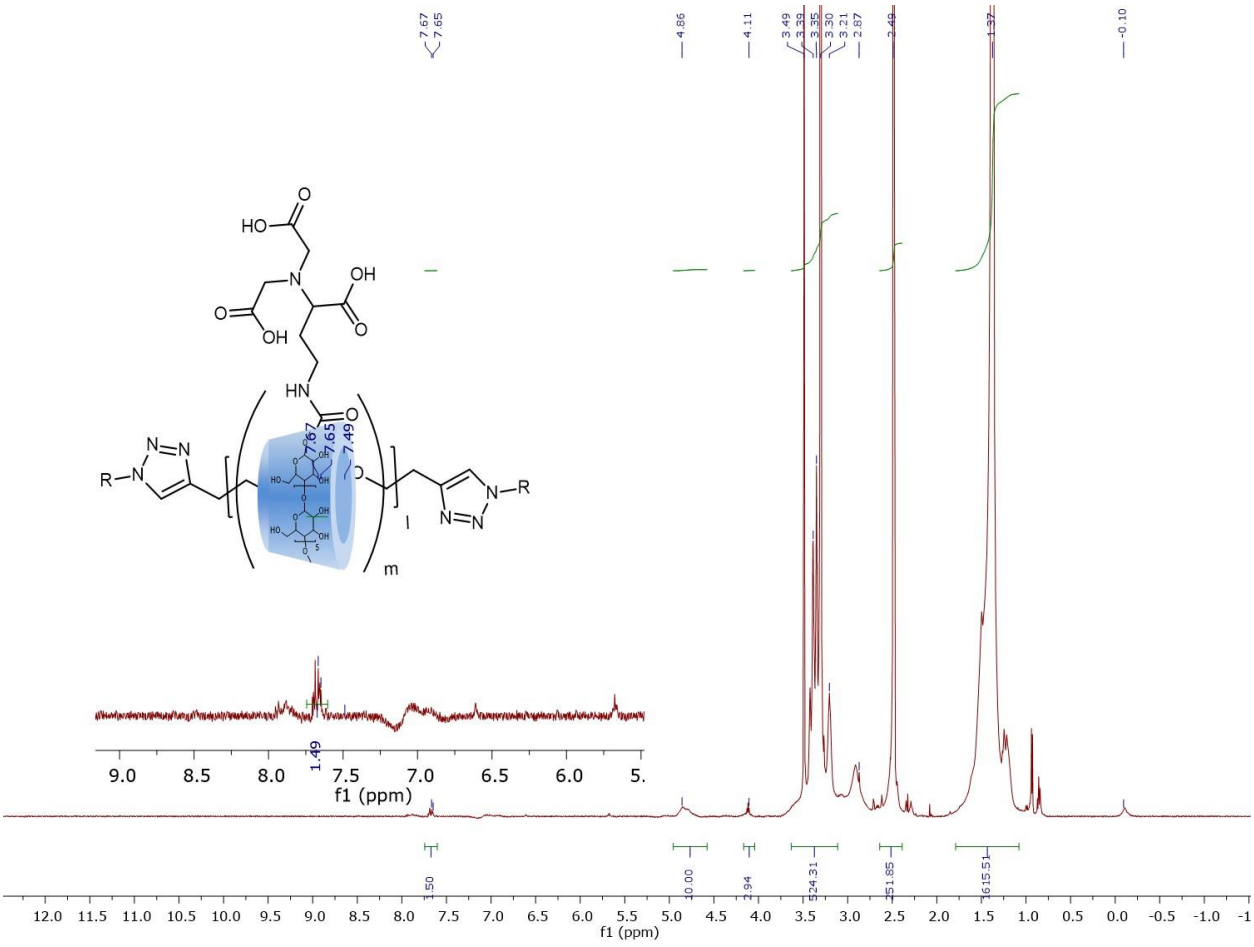

Figure 30: ^{1}H-NMR of Compound-11